Research Square

Preprints are preliminary reports that have not undergone peer review.
They should not be considered conclusive, used to inform clinical practice,
or referenced by the media as validated information.

An astrocyte-neuron HSPB1 axis preserves lysosomal integrity and protects from tau pathology

Maria Jimenez-Sanchez

maria.jimenez_sanchez@kcl.ac.uk

King's College London https://orcid.org/0000-0002-2287-1582

Paula Beltran Lobo

King's College London

Fangjia Yang

King's College London https://orcid.org/0009-0002-7967-0711

Cillian Power

University of Exeter https://orcid.org/0009-0002-5856-4303

Dorothea Böken

University of Cambridge https://orcid.org/0009-0008-8443-4469

Laure Verlin

King' College London

Roberto Guzman-Hernandez

King' College London

Sara Cantallops-Jimenez

King' College London

Saskia Pollack

King' College London

Abhiram Chakka

Queen Mary University of London https://orcid.org/0009-0000-9343-0162

James Crichton

University of Exeter

Jonathan Witton

University of Exeter https://orcid.org/0000-0001-9411-4022

Cara Croft

UK DRI https://orcid.org/0000-0001-7969-5084

David Klenerman

University of Cambridge https://orcid.org/0000-0001-7116-6954

Wendy Noble

King's College London. Institute of Psychiatry, Psychology & Neuroscience https://orcid.org/0000-0002-7898-4295

Article

Keywords:

Posted Date: October 12th, 2026

DOI: https://doi.org/10.21203/rs.3.rs-11192311/v1

License: This work is licensed under a Creative Commons Attribution 4.0 International License.
Read Full License

Additional Declarations: There is **NO** Competing Interest.

An astrocyte-neuron HSPB1 axis preserves lysosomal integrity and protects from tau pathology

Paula Beltran-Lobo[1], Fangjia Yang[1], Cillian Power[2], Dorothea Böken[3,4], Laure Verlin[1], Roberto Guzman-Hernandez[1], Sara Cantallops-Jimenez[1], Saskia J Pollack[1], Abhiram R Chakka[5], James C Crichton[2], Jonathan Witton[2], Cara L Croft[5], David Klenerman[3,4], Wendy Noble[2], Maria Jimenez-Sanchez[1,*]

[1]Department of Basic and Clinical Neuroscience, Maurice Wohl Clinical Neuroscience Institute, Institute of Psychiatry, Psychology and Neuroscience, King's College London, 5 Cutcombe Road, London, SE5 9RX, UK

[2]University of Exeter, Department of Clinical and Biomedical Sciences, Prince of Wales Road, Exeter, EX4 4PS, UK

[3]UK Dementia Research Institute, University of Cambridge, Cambridge, CB2 0AH, UK

[4] Yusuf Hamied Department of Chemistry, University of Cambridge, Cambridge, CB2 1EW, UK

[5]Centre for Neuroscience, Surgery & Trauma, The Blizard Institute, Faculty of Medicine and Dentistry, Queen Mary University of London, 4 Newark Street, London, E1 2AT, UK

*Corresponding author. Email: maria.jimenez_sanchez@kcl.ac.uk

Abstract

Alzheimer's disease (AD) is characterized by a decline in neuronal proteostasis that favours the accumulation of misfolded proteins. Molecular chaperones are essential to prevent protein aggregation and, although typically studied as intracellular proteins, chaperones can also be secreted with functions that remain to be elucidated. Here, we identify a mechanism by which astrocyte-secreted HSPB1 is internalized by neurons to increase neuronal proteostasis and prevent the aggregation of pathological tau. We characterized HSPB1 as an astrocytic protein that can also be acquired post-transcriptionally by neurons in AD brain and in culture. Upon internalization into the endolysosomal system through macropinocytosis, HSPB1 prevents lysosomal damage and promotes tau clearance, thereby positioning HSPB1 as a key protein in maintaining organelle and protein homeostasis across astrocyte-neuronal networks. This

work identifies a mechanism by which astrocytes boost neuronal capacity to protect from protein aggregation in neurodegeneration.

Introduction

Alzheimer's disease (AD), the most prevalent form of dementia, is neuropathologically defined by the presence of extracellular amyloid beta (Aβ) plaques and intracellular tau aggregates in the brain[1]. Cognitive decline in AD is closely linked to the accumulation of tau pathology, where its stereotypical spatial and temporal progression defines pathological staging and diagnosis[2]. Tau pathology involves its abnormal hyperphosphorylation, leading to its dissociation from microtubules and subsequent aggregation. In AD brain, tau aggregates accumulate within neurons in the form of neurofibrillary tangles (NFTs) and in degenerating axons and dendrites surrounding Aβ plaques as dystrophic neurites (DNs)[1].

Dysfunction of the autophagy-lysosomal system in neurons is increasingly recognized as a key contributor to the pathogenesis of neurodegenerative diseases[3]. In AD, Aβ[4] and tau pathology[5–7] have been associated with an impairment in lysosomal homeostasis. Autophagy is a conserved catabolic process that delivers cytoplasmic cargo to the lysosome for degradation. In addition to soluble proteins and aggregates, selective removal of damaged and dysfunctional organelles also plays a critical role in organelle quality control and neuronal health[8]. Extensive damage of lysosomes leads to their selective recognition by the autophagy machinery and removal by lysophagy[3,9].

The autophagy-lysosomal pathway works in coordination with molecular chaperones to maintain protein and organelle homeostasis. Recently, heat shock protein beta 1 (HSPB1) has been implicated in the maintenance of lysosomal integrity through its cooperation with the lysophagy machinery[10,11]. HSPB1 (also known as HSP27 in humans and Hsp25 in mice) is an ATP-independent chaperone belonging to the small heat shock protein (sHSP) family that function as holdases, preventing the aggregation of misfolded or aggregated proteins[12,13], including tau[14–16]. Notably, we have previously shown that HSPB1 is predominantly expressed in astrocytes of the frontal cortex in both healthy and AD human post-mortem tissue, where it is enriched in reactive astrocytes surrounding Aβ plaques[17]. However, the functional implications of HSPB1 in AD, particularly in reactive astrocytes, remain to be elucidated.

In neurodegenerative diseases, astrocytes shift to a reactive state characterized by functional, transcriptional and morphological changes[18]. We have previously shown that, in reactive conditions, astrocytes secrete proteins with molecular chaperone activity[19], including the chaperone HSPB1[17]. Importantly, we observed that astrocyte-secreted HSPB1 reduces the

accumulation of inclusions of pro-aggregant P301L/S320F mutant human tau in both mouse primary neuronal and organotypic brain slice cultures[17]. However, the mechanisms underlying this protective effect remain unknown. Here, we set out to investigate how an astrocyte-secreted chaperone can limit the accumulation of intraneuronal tau aggregates, and its relevance to human disease.

Our data support a protective role of astrocytic HSPB1 in AD, involving its uptake by neurons, followed by enhanced clearance of pathological tau. Immunohistochemistry and *in situ* hybridization in human brain, together with studies in mouse organotypic brain slice cultures support neuronal acquisition of astrocyte-specific HSPB1. These data may help explain why, despite being predominantly expressed by astrocytes, HSPB1 closely associates with tau pathology in human AD brain and in an *ex vivo* model of tauopathy. Using mouse primary neurons and neuronal cell lines, we characterized HSPB1 delivery to the endolysosomal system through macropinocytosis. Functionally, internalization of HSPB1 prevents loss of lysosomal integrity in response to damage. How does this explain the effect of extracellular HSPB1 on tau aggregation? We show that mutant tau inclusions are associated with increased lysosomal damage in neurons and that, conversely, inducing lysosomal damage further enhances tau aggregation. We propose that, by preserving lysosomal integrity, internalization of extracellular HSPB1 breaks this vicious cycle. Our results identify a novel mechanism by which extracellular HSPB1 is delivered to neuronal lysosomes to maintain their integrity under stress, such as in response to tau pathology, thereby facilitating its clearance and limiting its further aggregation.

Results

Accumulation of neuronal HSPB1 in AD is consistent with astrocytic HSPB1 transfer

To explore the relationship between HSPB1 and tau pathology in AD, we first examined HSPB1 protein levels across Braak stages of AD severity[2]. In the frontal and temporal cortices, regions affected relatively late and early in AD respectively, HSPB1 levels were significantly elevated in Braak V-VI cases compared to those with minimal or no tau pathology (Braak 0-II) (Fig. 1A-C). These results are in line with a meta-analysis of proteomic studies of the AD brain, which identified HSPB1 among the five most consistently upregulated proteins in AD[20].

Cell-type specific changes in HSPB1 protein levels were determined with triple immunostaining for HSPB1, aldehyde dehydrogenase 1 family member (ALDH1L1) as pan-astrocyte marker, and microtubule-associated protein 2 (MAP2) as a neuron-specific protein. The majority of HSPB1-positive cells (control: 98.23%±0.88, AD: 95.39%±1.72) were

astrocytes (Fig. 1D,E). While only a small fraction of HSPB1-positive cells corresponded to neurons, this percentage significantly increased from 1.73%±0.90% in control to 4.22%±1.04 in Braak V-VI AD (Fig. 1D,E). In addition to staining cell bodies, HSPB1 was frequently observed in blood vessels that may correspond to either astrocyte end-feet or endothelial cells, also reported to express HSPB1[21] (Fig. 1D, arrowheads), but these structures were excluded from the quantification. To assess changes in HSPB1 protein levels across cell types, we measured HSPB1 intensity in astrocytes (Fig. 1F,G) and neurons (Fig. 1H,I), which was significantly upregulated in both cell types in severe AD compared to controls. Thus, while HSPB1 protein expression is predominantly astrocytic, its levels are upregulated across cell types in AD, with a relative increase in the proportion of neuronal HSPB1.

To characterize cellular specific changes in *HSPB1* at the mRNA level, we next performed sensitive *in situ* hybridization using BaseScope, a variation of RNAscope that enables the detection of short (50-300 bp) mRNA sequences using a 'ZZ' probe, avoiding closely related pseudogenes, followed by signal amplification (Fig. S1A). This was combined with immunofluorescence using astrocyte- or neuronal-specific markers. We first confirmed successful detection of *HSPB1* mRNA along with the highly expressed ubiquitin C (*UBQ-C)* mRNA as a positive control, while no signal was detected for the bacterial mRNA dihydrodipicolinate reductase *(DapB)* in human tissue sections (Fig. S1B). In line with our observations at the protein level, cells containing *HSPB1* mRNA largely corresponded to ALDH1L1 positive astrocytes (Fig. S1C-D) and only a small fraction corresponded to NeuN positive cells (Fig. S1E-F). The number of astrocytes containing *HSPB1* mRNA increased in severe AD (Fig. 1J,K), which suggests an astrocytic HSPB1 transcriptional response in disease. In contrast, the number of NeuN positive neurons containing *HSPB1* mRNA decreased in AD compared to control cases (Fig. 1J,L). While HSPB1 protein levels are increased in AD in both astrocytes and neurons, our data indicate that this increase is transcriptionally driven only in astrocytes, suggesting that, in severe AD, neurons increased the levels of HSPB1 protein through post-transcriptional mechanisms.

We hypothesized that the increase in neuronal HSPB1 in AD might arise from the uptake of astrocyte-secreted HSPB1[17]. To explore this, we took advantage of our previously described *ex vivo* approach, where recombinant adeno-associated viruses (AAVs) drive astrocyte-specific human HSPB1 (hHSPB1) expression and secretion under the GFAP promoter (AAV-GFAP-hHSPB1) in organotypic brain slices[17] (Fig. 1M). Human-specific HSPB1 antibodies showed that, while hHSPB1 is predominantly observed in astrocytes, a small proportion of neurons also contain hHSPB1 (Fig. 1N). These findings support the neuronal uptake of

astrocyte-derived HSPB1 as a potential mechanism underlying the increased in neuronal HSPB1 protein observed in AD.

Astrocytic HSPB1 associates with neuronal tau pathology in human AD brain

We previously showed that extracellular HSPB1 reduces tau inclusions *in vitro* and *ex vivo*[17]. To determine whether astrocytic HSPB1 could exert this effect by associating with neuronal tau pathology, we co-transduced brain slices with AAVs to express hHSPB1 in astrocytes together with human tau bearing two pro-aggregant mutations (P301L/S320F-htau-EGFP), which forms tau sarkosyl-insoluble inclusions in neurons[17,22] (Fig. 2A,B). Notably, despite its astrocyte-specific expression, hHSPB1 was also detected in the tau sarkosyl-insoluble fraction (Fig. 2B,C). This was further confirmed in similar fractionation experiments using post-mortem frontal cortex spanning Braak III-VI AD cases as described in Beltran-Lobo et al.[23]. Immunoblotting with antibodies for tau phosphorylated at Ser396/Ser404 (PHF-1) or total tau, confirmed that phosphorylated insoluble tau species accumulate in the sarkosyl-insoluble rather than the sarkosyl-soluble fraction (Fig. 2D). The majority of HSPB1 accumulated in the sarkosyl-soluble tau fraction, where its levels positively correlated with soluble total tau across cases (Fig. 2D, E). Notably, HSPB1 was also found in the sarkosyl-insoluble tau fraction and positively correlated with PHF1-positive insoluble tau (Fig. 2D,F).

To confirm the spatial association between HSPB1 and tau pathology within neurons, a Ser202/Thr205 phosphorylated tau antibody (AT8) was used to detect tau pathology in human brain temporal cortex sections from severe AD cases through immunofluorescence. Regions containing dystrophic neurites (DNs) or equivalent regions with no pathological tau lesions (NLs) (Fig. 2G) were selected. We observed an enrichment of GFAP-positive reactive astrocytes in regions containing DNs (Fig. 2H), where HSPB1 co-localized with GFAP-positive astrocytes (Fig. 2I) and phosphorylated tau (AT8) (Fig. 2J). To specifically assess the association of HSPB1 with pathological tau in neuronal cell bodies, we quantified the proportion of neurons harbouring pathological AT8 in neurofibrillary tangles (NFTs) (16.01 ± 5.27%) (Fig. 2K,L), of which 10.98 ± 5.47% were also positive for HSPB1 (Fig. 2K,M). These data indicate that, although HSPB1 is predominantly an astrocytic protein, it is associated with two major hallmarks of tau pathology in AD, DNs and NFTs. These findings suggest that astrocyte-derived HSPB1 accumulates in neurons and highlight an association between increased HSPB1 levels and tau pathology in AD.

Neuronal internalization of extracellular HSPB1 is mediated by macropinocytosis

To further establish the mechanism that mediate neuronal internalization of extracellular HSPB1, we first used SH-SY5Y neuroblastoma cells to efficiently express markers of early (Rab5-mRFP) and late (Rab7-mRFP) endosomes. Upon addition of recombinant human HSPB1 labelled with Oregon Green (rhHSPB1-OG) to the extracellular medium, live cell imaging revealed cytoplasmic puncta positive for both rhHSPB1-OG and Rab5 (13.3% ±0.78) (Fig. 3A-C) or Rab7 (8.9%±4.68) (Fig. 3D-F).

Next, we investigated the endocytic pathway responsible for HSPB1 internalization using pharmacological inhibitors and live confocal imaging of rhHSPB1-OG. Inhibition of clathrin-mediated endocytosis pathways with dynasore and chlorpromazine (CPZ)[24,25] for 30 min, followed by 1h treatment with rhHSPB1-OG, partially reduced the number of rhHSPB1-OG puncta per neuron (Fig. 3G,H). Strikingly, 5-N-ethyl-N-isopropyl amiloride (EIPA), an inhibitor of Na+/H+ exchanger that is classically used to block macropinocytosis[26], drastically suppressed HSPB1 internalization (Fig IJ). Consistent with an actin-dependent process, latrunculin A (LatA), an inhibitor of actin polymerization[27], also significantly impaired HSPB1 uptake (Fig 3I,J). Collectively, these findings indicate that while other endocytic pathways may contribute, internalization of extracellular HSPB1 is predominantly actin-dependent and driven by macropinocytosis.

To determine the fate of HSPB1 following endocytosis, primary neurons were exposed to rhHSPB1-OG followed by treatment with the lysosomal inhibitor Bafilomycin A1[28]. rhHSPB1-OG positive puncta accumulation within acidic compartments labelled by LysoTracker was significantly increased (Fig. 3K,L), supporting the endocytic internalization and lysosomal trafficking of extracellular HSPB1. These findings are consistent with our previous observations[17], showing that >80% of internalized HSPB1 was found within LysoTracker-positive compartments. The internalization of astrocyte-secreted HSPB1 was further confirmed by exposing primary neurons to conditioned media (ACM) from astrocytes expressing human EGFP-HSPB1 (EGFP-hHSPB1) (Fig. S2C-D) and showing that hHSPB1 largely colocalized with endogenous Lamp1-positive structures in neurons (Fig. S2E).

Internalization of HSPB1 preserves lysosomal integrity upon lysosomal damage

The delivery of astrocyte-secreted HSPB1 to lysosomes prompted us to examine its potential role in lysosomal function. Intracellular HSPB1 has recently been implicated in lysosomal homeostasis by facilitating clearance of damaged lysosomes[10,11]. To determine whether internalized HSPB1 similarly contributes to lysosomal integrity, we induced lysosomal damage using L-Leucyl-L-Leucine methyl ester (LLOMe), a well-stablished lysosomotropic agent that permeabilizes lysosomal membranes[9]. As expected, treatment of SH-SY5Y cells with low

concentrations of LLOMe (50uM, 1h) was sufficient to markedly reduce the number of functional lysosomes, evidenced by a decreased lysosomal acidification monitored by LysoTracker staining (Fig. 4A,B). Pre-treatment with extracellular rhHSPB1 for 1h, partially rescued LLOMe-induced lysosomal dysfunction, while having no effect in basal conditions (Fig. 4A,B). Lysosomal membrane damage can be monitored by the recruitment of cytoplasmic galectins such as galectin-3 (Gal3), which bind the luminal β-galactosidase upon membrane rupture[9]. Consistent with this, LLOMe triggered a rapid recruitment of cytoplasmic mCherry-Gal3 to damaged lysosomes. Notably, the number of Gal3-positive damaged lysosomes was significantly reduced in cells pre-treated with rhHSPB1 (Fig. 4C,D), without affecting the total number of Lamp1-mCherry-positive lysosomes (Fig. 4E,F). Together, these findings indicate that extracellular HSPB1 confers protection against lysosomal damage induced by general lysosomal stress.

Interestingly, HSPB1 was previously identified as a Gal3 interactor during LLOMe-induced lysosomal damage[29,30]. Consistent with this, we found that HSPB1 co-immunoprecipitates with either endogenous or overexpressed Gal3, and this interaction was enhanced by LLOMe treatment and by addition of rhHSPB1 to the medium, suggesting that both endogenous and extracellular HSPB1 associate with Gal3 upon lysosomal damage (Fig S3A-C). To specifically distinguish internalized from endogenous HSPB1, we next used live-cell imaging to track exogenously added HSPB1 and examine its association with damaged lysosomes. Cells treated with rhHSPB1-OG followed by LLOMe displayed an increase in vesicles containing both mCherry-Gal3 and rhHSPB1-OG (Fig. 4G,H), while there were no changes in the number of Lamp1-mCherry vesicles containing rhHSPB1 (Fig. 4I,J). Our data suggests that internalized HSPB1 interacts with Gal3 at damaged lysosomes, coinciding with reduced lysosomal damage and improved lysosomal integrity.

Gal3 recruitment to damaged lysosomes facilitates lysosomal clearance by recruiting the components of the autophagy machinery for lysophagy[9]. Consistent with this, LLOMe-induced lysosomal damage in SH-SY5Y cells for 1h increased the number of mCherry-LC3-positive puncta (Fig 5A,B). Pre-treatment with extracellular rhHSPB1 led to a modest but significant increase in LC3 vesicles in LLOMe-treated cells, while no changes were observed in control cells (Fig. 5A,B). A proportion of vesicles containing mCherry-LC3 were also positive for rhHSPB1-OG, which showed a trend towards an increased upon LLOMe exposure (Fig. 5C,D), suggesting that internalized rhHSPB1 may facilitate autophagosome formation during lysosomal damage. In our conditions we did not observe changes in the number of mCherry-p62 puncta (Fig. 5EF), a recently described lysophagy adaptor and interactor of endogenous HSPB1[11].

Exogenous HSPB1 prevents the formation of long tau aggregates

We previously reported that extracellular HSPB1 reduces tau pathology burden in mouse primary neurons and organotypic brain slice cultures expressing human tau carrying the P301L and S320F mutations (P301L/S320F-htau-EGFP)[17]. To better understand the effects of extracellular HSPB1 on neuronal tau pathology, we evaluated its effects on the composition of intracellular tau aggregates using single-molecule techniques employed recently to characterize tau aggregate composition and formation in neurons expressing P301L/S320F-htau[31,32]. We first quantified the proportion of soluble tau present as aggregates in neurons expressing WT-htau or mutant P301L/S320F-htau using a single-molecule array (SIMOA) immunoassay that employs a sandwich configuration with either a total human tau (HT7-HT7) or a phospho-tau antibody (AT8-AT8) (Fig. 6A)[31]. Neurons expressing mutant htau accumulated soluble HT7-positive tau aggregates over time (from 15.52ng/mL±10.60 at 8 DIV to 72.14ng/mL±22.35 at 12 DIV) (Fig. 6B), yet their levels were not altered by addition of rhHSPB1 to the medium at any time point. In contrast, AT8-positive aggregates showed an increasing trend upon HSPB1 treatment at 12 DIV (23.73ng/mL±3.1) relative to vehicle (31.12ng/mL±5.2) in neurons expressing mutant htau (Fig. 6C). To better understand the effect of internalized HSPB1 on individual tau aggregates in the tens to hundreds of nanometers range, we applied single-molecule pull-down assay (SiMPull)[33]. For this, tau aggregates were captured using a HT7 antibody and detected with a DNA-labelled HT7 antibody, followed by super-resolution microscopy (DNA-PAINT) (Fig. 6D), providing detailed information on individual aggregate shape and size[34,32]. HSPB1 treatment did not alter the overall proportion of total fibrillar tau aggregates in neurons expressing WT or mutant htau (defined as those with eccentricity (>0.9); Fig. 6E-G). However, HSPB1 significantly reduced the proportion of long aggregates (defined as those with length >150 nm) in neurons harbouring mutant htau in comparison to the levels detected in vehicle treated neurons (Fig. 6H). This supports a protective role of extracellular HSPB1 on tau pathology in neurons, particularly by reducing long fibrillar tau aggregates.

Internalized HSPB1 prevents tau-induced lysosomal damage and reduces tau levels

To explore the mechanisms by which internalized HSPB1 reduces tau pathology, we assessed tau phosphorylation at PHF1 in neurons treated with exogenous HSPB1 and observed no changes that could potentially explain its effect on aggregation (Fig. S4A-C).

Internalized HSPB1 was recruited to cells expressing either WT or mutant htau in a similar manner (Fig. S4 D, E) and was only found in endolysosomal structures, with no apparent HSPB1 in the cytoplasm (Fig. 3). Thus, we next investigated whether HSPB1-mediated

protection against tau aggregates is linked to its recruitment to endolysosomal structures and maintenance of lysosomal integrity in htau expressing neurons. To assess lysosomal damage, the detection of endogenous Gal3 puncta was assessed by immunofluorescence in primary neurons expressing pro-aggregant mutant P301L/S320F-htau-EGFP for 6 days and compared to neurons expressing WT-htau-EGFP. While Gal3 displayed a mostly diffuse pattern in both conditions, the proportion of cells containing Gal3 puncta was markedly higher in neurons expressing mutant htau (Fig. 7A,B). Within mutant htau expressing neurons, Gal3 puncta were predominantly observed in neurons that also contained htau inclusions (Fig. 7C), indicating that, intracellular tau aggregation drives lysosomal damage.

Concomitantly, lysosomal damage induced by LLOMe exposure for 6h increased the proportion of neurons containing mutant htau inclusions (Fig. 7D,E). These findings suggest a vicious cycle, where mutant htau enhances lysosomal damage, which impairs lysosomal degradation capacity, leading to further accumulation and aggregation of mutant htau. We hypothesized that preventing lysosomal damage through internalized HSPB1 could break this cycle and increase tau clearance to reduce mutant htau aggregates.

To test this, we examined the effect of extracellular rhHSPB1 on tau degradation rates. SH-SY5Y cells expressing either EGFP-tagged WT or P301L mutant htau, were treated with cycloheximide to inhibit protein synthesis, and tau clearance was measured over time in the presence of rhHSPB1 or vehicle control. In both cases, we observed that treatment with rhHSPB1 significantly reduced htau levels by 24h (Fig. 7F,G), supporting a model where the uptake of HSPB1 enhances tau clearance by preserving lysosomal function.

Expression of HSPB1 in astrocytes enhances clearance of mutant tau in neurons

To further assess how the astrocyte-neuron HSPB1 axis regulates tau turnover, we used organotypic brain slices expressing htau tagged with a green-to-red photoswitchable fluorescent protein[35]. Mouse organotypic brain slices where transduced with AAV-GFAP-hHSPB1, which enables human HSPB1 expression in astrocytes as well as its secretion[17], or AAV-GFAP as a control, together with AAVs expressing Dendra2-tagged WT or mutant P301L/S320F-htau and which result in htau expression in MAP2-positive neurons (Fig. S5A). Photoconversion from green to red fluorescence occurs following a brief 405 nm pulse and, sequential imaging of red fluorescence signal immediately after photoconversion and up to day 21, allows monitoring of tau half-life (Fig. S5A). This can be distinguished from htau protein synthesis, monitored by the green fluorescence of non-photoconverted protein (Fig. S5B,C).

Brain slices expressing astrocytic hHSPB1 showed no changes in red fluorescent decay for WT htau compared to control slices (Fig. 8B,C). In contrast, a significant reduction in P301L/S320F-htau red fluorescence signal was detected at 14 days after photoconversion, alongside reduced mutant tau half-life (Fig. 8D,E), pointing towards a role of astrocytic hHSPB1 in accelerating mutant htau turnover *ex vivo*. Concomitantly, brain slices transduced with AAV-GFAP-hHSPB1 showed an increased mutant tau photoconversion ratio, where values above 1 indicate faster photoconverted signal loss and increased tau turnover. No significant changes were observed for WT-htau (Fig. 8F).

These data provide a mechanistic explanation for our previous observation that astrocytic hHSPB1 reduces tau pathology in neurons[17], preventing the formation of long fibrillar tau aggregates. Our findings highlight a protective mechanism whereby astrocyte-secreted HSPB1 is internalized into the neuronal endolysosomal compartment, where it protects lysosomes from damage and thereby facilitates tau clearance, contributing to protection against neuronal tau aggregation in AD (Fig. 8G).

Discussion

Maintenance of neuronal proteostasis is essential for preventing the life-time accumulation of misfolded proteins and damaged organelles that contribute to neurodegeneration. Here, we propose a mechanism by which astrocytes supply neurons with protective chaperones to maintain organelle and protein homeostasis thereby protecting against protein aggregation via astrocyte-neuron interactions. We have provided evidence from human post-mortem brain tissue, *ex vivo* organotypic brain slice culture models and primary cultures *in vitro* to demonstrate that neurons internalize the chaperone HSPB1. Internalized HSPB1 is directed to the endolysosomal compartment where it maintains lysosomal integrity, which in turn, enhances tau clearance and limits its aggregation into long aggregates.

Ageing and neurodegenerative conditions are characterized by a decline in brain proteostasis capacity[36,37]. Interestingly, while mRNA levels of chaperones generally decrease in ageing and neurodegeneration, the chaperone family of small heat shock proteins (sHSPs) are upregulated transcriptionally[38]. This is very noticeable for HSPB1, which is found amongst the top five upregulated proteins in AD brain across proteomic studies[20]. Our data confirmed the upregulation of HSPB1 protein in AD and further revealed that such increase is largely mediated by elevated HSPB1 mRNA and protein expression in astrocytes. This is consistent with transcriptomic studies at the single cell level that identified HSPB1 and other sHSPs within the upregulated genes in astrocytes in human AD brain[39–43]. Altogether, this evidence points towards a resilience mechanism in astrocytes that counteracts the general disease-associated

decline in chaperone levels through the upregulation of specific chaperones, such as those of the sHSP family. Thus, increasing chaperone levels may represent a mechanism by which astrocytes boost their cell autonomous proteostasis capacity. In addition, and not mutually exclusive, our data support a non-cell autonomous role by which astrocytes supply neurons with chaperones to compensate for the disease- and age-dependent decline in proteostasis capacity in neurons.

The concept of chaperones as mediators of glia-neuron interactions was first proposed more than forty years ago[44] and more recently supported by studies in mouse and fly models of Huntington's disease[45–47], cellular models of amyotrophic lateral sclerosis (ALS)[48], ageing in *C. elegans*[49] and in our own work in cellular and organotypic brain slice models of tau pathology[17]. By combining single-cell immunohistochemistry and *in situ* hybridization analysis in AD tissue, our data support the hypothesis that chaperone transfer from astrocytes to neurons occurs in human disease. Furthermore, our findings provide a potential mechanistic explanation for how HSPB1, despite being predominantly expressed in astrocytes, localizes to AT8-positive DNs and NFTs and associates with insoluble tau aggregates in human AD brain. Internalization of chaperones has been reported in several contexts[50], although the routes underlying their uptake are not completely understood. Here, we show that neurons primarily internalize HSPB1 through macropinocytosis which, interestingly, is also the largest reported route for tau uptake[51–53]. Although less prominent, clathrin-mediated endocytosis, which likewise has been described as a route for tau internalization[54], also contributes to HSPB1 uptake to a lesser extent.

Our previous studies showed that astrocyte-secreted and extracellular HSPB1 lowers the proportion of neurons bearing tau aggregates[17]. We further characterized the effects of internalized HSPB1, showing that it specifically reduces the abundance of long tau fibrils using a single molecule pull down assay that allows monitoring disease specific tau aggregates with high specificity and sensitivity[31,33,34]. This prompted us to investigate the mechanisms that mediate such effect. HSPB1 has been largely linked to tau pathology via direct interactions. Several studies supported HSPB1 co-localization with phosphorylated tau in human brain[55,56] and in neurons over-expressing HSPB1 in *Drosophila* and mouse models of tauopathy[14,56], as well as HSPB1 interactions with tau and inhibitory action on its aggregation *in vitro*[14–16,56,57]. However, in our experimental models, internalized HSPB1 seemed restricted to the endolysosomal compartment, preventing it from interacting with the main pool of tau in the neuronal cytoplasm, which prompted us to investigate alternative mechanisms.

Tau pathology has been extensively linked to lysosomal stress through both the direct effects of intracellular tau on lysosomal function[6] and damage of the endolysosomal membrane

following the internalization of exogenous tau seeds[58,59]. Damage of the lysosomal membrane compromises the functionality of this organelle[3,9]. Indeed, neurons expressing mutant htau displayed increased lysosomal damage sensed by Gal3. In turn, neurons treated with the lysosomotropic agent LLOMe, showed an increase in the accumulation of tau aggregates, highlighting a feed-forward loop between deficient lysosomal function and tau aggregate load. Given that tau pathology has been linked to impairment of the autophagy lysosomal pathway[5–7] and that, conversely, aggregated tau species can be cleared via this pathway[60–68], we proposed that internalized HSPB1 could reduce tau pathology by maintaining lysosomal integrity and functionality and enhancing tau degradation. A novel role of HSPB1 on lysosomal integrity has been recently described[10,11], implicating HSPB1 as a regulator of p62 phase transition and facilitator of lysophagy[10,11]. Specifically, p62 has been shown to act as a lysophagy adaptor that forms phase condensates on damaged lysosomal membranes to recruit autophagy components, while also recruiting endogenous HSPB1 to damaged lysosomes to maintain the p62 condensate liquidity and facilitate lysophagy[11]. Several autophagy adaptors have been identified in lysophagy, including NDP52, TAX1BP1 and p62[11,30,69–71], providing evidence for both p62-dependent and -independent lysophagy. While a more in-depth investigation on the potential implications of p62 is required, our data do not show changes in p62 upon HSPB1 internalization. This may suggest that the specific role of HSPB1 on lysophagy differs depending on whether HSPB1 is intracellular or acquired from the extracellular space. This could potentially lead to differential locations and subsequent functions of HSPB1 within subcellular compartments.

Beyond tau, these findings could be relevant to other neurodegenerative diseases linked to lysosomal damage, including those that accumulate a-synuclein[72,73] or TDP-43[74]. Overall, this mechanism reveals HSPB1 as a key astrocytic protein that serves as a mediator of astrocyte-neuron communication to preserve lysosomal integrity and boost neuronal proteostasis.

Materials and Methods

Methods

Post-mortem human brain

Post-mortem human prefrontal cortex Brodmann area 9 (BA9) and temporal cortex (BA21) from age-, gender- and post-mortem delay matched non-neurologically impaired donors (Braak stage 0-II) and pathologically confirmed cases of sporadic moderate AD (Braak stage III-IV) and severe AD (Braak stage V-VI) were obtained from the London Neurodegenerative Diseases Brain Bank at King's College London (Tables S1, S2). All tissue donations were

collected with informed consent for use in research, and this study was conducted under the ethical approval of the tissue bank (23/WA/0124 Wales REC 3, Registration Date 17/05/2023).

Total human brain homogenisation

Brain homogenates were prepared as described[23]. In brief, 100 mg frozen post-mortem grey matter from AD (n = 20 BA9, n = 9 BA21) and control (n = 10 BA9, n = 4 BA21) brain was mechanically homogenised in 1mL of ice-cold lysis buffer containing 10 mM Tris-HCl (pH 7.5), 75 mM NaCl, 0.5 % sodium dodecylsulphate (SDS) (w/v), 20 mM sodium deoxycholate and 1 % (v/v) Triton-X-100 supplemented with 10 mM ethylenediaminetetraacetic acid (EDTA), protease (Roche, 11697498001) and phosphatase inhibitors (Roche, 4906845001). After 10 seconds sonication, samples were centrifuged at 25,000 g for 20 min at 4 ºC.

Human brain immunofluorescence

Temporal cortex 7 µm-thickness sections of human AD and control brain were prepared from formalin-fixed paraffin-embedded (FFPE) as previously described [17]. Sections were deparaffinized in xylene (Thermo Fisher Scientific, X/0250/17) and rehydrated in 99% (v/v) ethanol, followed by anti gen retrieval in citrate buffer (0.01 M sodium citrate, pH 6) at 95° to 100°C for 5 min and 65°C for 12 min. Sections were cooled in water and rinsed in tris-buffered saline (TBS). After drawing a hydrophobic barrier around the tissue, sections were incubated in blocking buffer [1:100 normal goat serum (Sigma-Aldrich, G9023) in TBS] followed by the incubation with the corresponding primary antibodies overnight: ALDH1L1 (1:200, Antibodies-online, ABIN1304519), AT8 (1:200, Invitrogen, MN1020), GFAP (1:500, Abcam, ab4674), HSPB1 (1:200, Enzo, ADI-SPA-803), MAP2 (1:500, GeneTex, GTX82661). Sections were washed three times in TBS and incubated with secondary anti-mouse or anti-rabbit antibodies conjugated to Alexa Fluor 488 (ThermoFisher, A-11008) or 568 (ThermoFisher, A-11004) or anti-goat conjugated to Alexa 647 (Abcam, ab150175) at 1:250. Autofluorescence was then quenched using 0.3% (w/v) Sudan Black (Acros Organics, 190160250) in 70% ethanol for 10 min and sections were mounted in Fluoromount-G mounting medium with 4′,6- diamidino- 2- phenylindole (DAPI) (Invitrogen, 00- 4959- 52). Sections were imaged on an Olympus SlideView VS200 at 20x magnification.

Analysis of human brain immunofluorescence

QuPath and Fiji were employed for the colocalisation analysis of HSPB1 and tau lesions. For this, forty 140.6x106.6 µm regions of interest (ROIs) within the grey matter of AD sections containing AT8-positive dystrophic neurites (DN) in the centre of the ROI were defined per

case. ROIs with no AT8 immunopositive lesions (NL) were used as control. Following image thresholding, GFAP integrated density was measured per ROI and colocalisation between HSPB1 and GFAP or AT8 signals was determined using the FIJI plugin JACoP (Just Another Co-localization Plugin).

To determine the proportion of HSPB1-positive cells that are astrocytes or neurons, 20–25 ROIs measuring 422 × 320 µm were randomly selected across the grey matter. Within each ROI, HSPB1-positive cells were selected and subsequently classified as ALDH1L1+ or MAP2+. A minimum of 500 HSPB1-positive cells were counted across the selected ROIs. The percentage of HSPB1-positive cells classified as astrocytes or neurons was then calculated relative to the total number of HSPB1-positive cells per case.

Quantification of HSPB1 fluorescence intensity in neurons and astrocytes was performed in Fiji. Images were thresholded to select ALDH1L1-positive or MAP2-positive cells, and a binary mask was generated to identify astrocytes or neurons, respectively. Between 20-25 ROIs were defined, containing between 300-360 ALDH1L1-positive astrocytes or 107-160 MAP2-positive neurons per case. The mean HSPB1 fluorescence intensity was measured within each single-cell ALDH1L1 or MAP2 object.

To assess the association between HSPB1 and neuronal tau pathology, twenty ROIs of 420x321 µm were defined per AD case. The percentage of AT8-positive neurons was calculated from a minimum of 500 MAP2-positive neurons per case. The percentage of HSPB1-positive neurofibrillary tangles (NFTs) was calculated from a minimum of 100 AT8-positive NFTs per case.

In-situ hybridisation and immunofluorescence in human brain

Temporal cortex 5 µm-thickness sections from control and AD were prepared from FFPE blocks. In-situ hybridisation (ISH) was performed using BaseScope 2.5 High Definition – RedAssay (ACDbio). In brief, slides were baked in hybridiser HB-1D oven (Akribis Scientific Limited) at 60ºC for 30 min. FFPE-sections were deparaffinised in xylene and 100 % ethanol. After drying the slides for 5 min at RT, H_2O_2 (pre-treatment 1) was added for 30 min. Slides were incubated in 90–100ºC antigen retrieval solution (pre-treatment 2) for 30 min, washed in distilled water twice, dehydrated using 100 % ethanol and treated with protease IV (pre-treatment 3) for 30 min at 40ºC prior to two further washes in distilled water. FFPE-fixed sections were incubated with the HSPB1 mRNA probes for 2 h at 40ºC after which samples were washed twice in 1X washing buffer**.** Signal amplification was performed by a series of incubations using eight amplification probes (Amp1-8) for alternating periods of 30

(Amplification 1,2,4,5) and 15 (Amplification 3 and 6) min at 40ºC or room temperature (Amp7-8) as indicated by the supplier. Detection was performed by incubating the FFPE sections with a substrate mixture of RED-A and RED-B (1:60 ratio) for 10 min at room temperature protected from light. Tap water was used to remove excess substrate.

After HSPB1 mRNA detection by BaseScope, sections underwent IHC following a previously described method [23]. In brief, hybridised sections were washed twice in PBS and non-specific antibody binding blocked with 2.5 % (v/v) normal horse serum (NHS) (Vectorlabs) for 2h at RT for labelling with antibodies against ALDH1L1 (1:100, Antibodies-online ABIN1304519) or NeuN (1:50, Millipore ABN78). Tissue sections were incubated overnight at 4ºC with primary antibodies diluted in 1 % (v/v) NHS in PBS. Following PBS washing, sections were incubated with fluorophore-conjugated secondary antibodies secondary antibodies conjugated to Alexa Fluor 488 (ThermoFisher, A-11001 or A-11008) at 1:200 in 1 % (v/v) NHS for 1 h at room temperature. Sections were rinsed in PBS and autofluorescence was quenched using TrueBlack (Biotinum, BT23007) diluted 1:20 in 70 % ethanol for 30 seconds. Slides were washed five times in PBS before mounting in Fluoromount-G mounting medium with DAPI.

To assess the number of astrocytes and neurons containing HSPB1 mRNA puncta, QuPath was used for cell detection and quantification. ROIs measuring 46,960.046 μm² were defined across the grey matter. Cells were identified using the cell detection tool based on DAPI-stained nuclei. Between 119 and 272 ALDH1L1-positive astrocytes and 53–87 NeuN-positive neurons were detected per case. Cell boundaries were then approximated by applying a 10 μm radial expansion from each detected nucleus using the cell expansion parameter, thereby defining the cellular area for subsequent quantification of cell types positive for HSPB1 mRNA puncta. A minimum of fifty HSPB1 mRNA-positive cells were counted per case. The percentage of astrocytes or neurons containing HSPB1 mRNA puncta relative to the total number of corresponding cell types counted per case was then calculated. To determine the proportion of HSPB1 mRNA-positive cells labelled as ALDH1L1-positive astrocytes or NeuN-positive neurons, 100 or 200 HSPB1 mRNA-positive cells per staining type, respectively, were manually selected per case. A 10 μm radial expansion from the detected nucleus was applied to define the cellular boundaries, after which cells were classified as ALDH1L1-positive or NeuN-positive based on immunolabelling. The percentage of HSPB1 mRNA-positive cells classified as either astrocytes or neurons was then calculated relative to the total number of HSPB1 mRNA-positive cells.

Recombinant AAVs

AAV8-GFAP and AAV8-GFAP-hHSPB1 were obtained from VectorBuilder by packaging pAAV[Exp]-GFAP(short)>TagBFP2:WPRE and pAAV[Exp]-GFAP(short) >hHSPB1[NM001540.5]:P2A:TagBFP2:WPRE into single-stranded AAV8 viruses[17]. AAV2/TM8-CBA-WT-htau0N4R-EGFP (WT-htau-EGFP), AAV2/TM8-CBA-P301L/S320F-htau0N4R-EGFP (P301L/S320F-htau-EGFP), AAV2/TM8-SYN-WT-htau0N4R (WT-htau) and AAV2/TM8-SYN-P301L/S320F-htau0N4R (P301L/S320F-htau)[22], and AAV2/TM8-CBA-WT-htau0N4R-Dendra2 (WT-htau-Dendra2) and AAV2/TM8-CBA-P301L/S320F-htau0N4R-Dendra2(P301L/S320F-htau-Dendra2)[35] were obtained by microscale preparation[22].

Recombinant HSPB1 and reactive dye labelling

rhHSPB1 (R&D Systems, 1580-HS) stock solution was diluted in 0.1% (w/v) bovine serum albumin (BSA) in phosphate-buffered saline (PBS). For reactive dye labelling, the manufacturer stock solution of was exchanged to 0.1 M sodium bicarbonate (pH 8.3) using a 3-kDa column concentrator (Millipore, UFC500396) and incubated with Oregon Green 488 dye (1 mg/ml; Thermo Fisher Scientific, O6149) or Alexa 568 NHS ester dye (10 mg/ml, Thermo Fisher Scienctific, A20003) for 1 h at room temperature. To wash the unbound dye, PBS was added onto the reaction mixture and then applied onto a previously equilibrated Zeba Spin desalting column (Thermo, 89890) and centrifuged at 1000 g for 2 min. The same steps without rhHSPB1 were followed to obtain the dye only control.

Animals

All animal work was conducted in accordance with the UK Animals (Scientific Procedures) Act 1986 Amendment Regulations 2021 under UK Home Office Personal and Project Licenses and approved by the King's College London or University of Exeter Animal Welfare and Ethical Review Boards.

Mouse organotypic brain slice cultures

Organotypic brain slice cultures (BSCs) were prepared from wild-type CD1 mice for sarkosyl extraction or C57BL/6J mice for Dendra-tau imaging at post-natal day 7, as previously described[17,23]. Brains were dissected in ice-cold oxygenated dissection buffer (124 mM NaCl, 3 mM KCl, 1.25 mM KH_2PO_4, 8.2 mM $MgSO_4$ $7H_2O$, 2.65 mM $CaCl_2$ 2H2O, 3.5 mM NaHCO3, 1.99 mM ascorbic acid, 10 mM glucose and 0.2 mg/mL ATP [Sigma-Aldrich, A6419]), and three sections of 350 µm thickness cut with a McIlwain tissue chopper (Stoelting, 51350) were placed on 0.4 µm Millicell culture inserts (Merck Millipore, 10412511) and culture in 1 mL of slice culture medium (19.3 mM NaCl, 5 mM $NaHCO_3$, 2.7 mM $CaCl_2$ $2H_2O$, 2.5 mM $MgSO_4$

$7H_2O$, 0.5 mM ascorbic acid, 9.19 g/L basal medium eagle [Sigma-Aldrich, H0887], 40 mM glucose, 1 mM HEPES, 5 U/mL penicillin-streptomycin [Sigma-Aldrich, 15140122], 0.33 mg/L insulin [Sigma-Aldrich, 9278] and 25 % (v/v) horse serum [Sigma-Aldrich, H1138] pH7).

Three hours after plating, the culture medium was replaced with 1 mL of pre-warmed fresh sterile culture medium. AAVs were diluted in the fresh media to express tau or HSPB1 using: AAV2/TM8 WT-htau-EGFP or P301L/S320F-htau-EGFP ($1x10^{11}$ VGs/ml), AAV2/TM8 WT-htau-Dendra2, P301L/S320F--Dendra2, AAV8-GFAP-BFP or AAV8-GFAP-BFP2:hHSPB1 ($1x10^{10}$ VGs/mL). The medium was replaced every 2-3 days until slices were harvested at 28 DIV or imaged at the indicated time points.

Sarkosyl extraction from human brain and organotypic slices

Sarkosyl-insoluble tau was isolated from 100 mg/mL post-mortem human brain (BA9) or a pool of 12 mouse organotypic brain slices cultures (BSCs) as previously[17,23]. Briefly, human brain or mouse BSCs were harvested in ice-cold homogenisation buffer (50 mM TBS, 10 % (w/v) sucrose, 2 mM EGTA, protease and phosphatase inhibitors (Roche)) and mechanically dissociated using a hand-held mechanical tissue homogeniser (Omni International) or a Teflon glass homogeniser, respectively. Following centrifugation at 4 ºC for 20 min at 13,000 g, the supernatant was collected as the low-speed supernatant, which was used as total lysate. N-lauroylsarcosine sodium salt solution (Sarkosyl, Sigma-Aldrich, L7414) was added to the remaining supernatant to a final concentration of 1% and this was incubated at ambient temperature for 30 min prior to centrifugation at 100,000 g for 1 h at 21ºC using an Optima MAX-XP ultracentrifuge (Beckman Coulter). The supernatant was collected as the high-speed supernatant containing sarkosyl-soluble tau. The pellet was washed with 1 % sarkosyl in homogenisation buffer and centrifuged at 100,000 g for 15 min at 21ºC. The pellet, containing sarkosyl-insoluble tau was resuspended in Laemmli buffer.

Dendra-2 imaging and analysis of tau turnover in brain organotypic slice cultures

Tau turnover was measured in slices expressing WT-htau-Dendra2 or P301L/S320F-htau-Dendra2[35]. Dendra2 was photoconverted using a pulse of blue (405 nm) light. Organotypic slices were imaged live using a Leica SP8 confocal microscope (LAS X, HC FLUOTAR L 25×/0.95 W VISIR water-immersion objective) at 37 °C, using sequential scanning with HyD detectors to prevent bleed-through between channels. Green (unconverted) Dendra2 was excited at 488 nm and collected at 500 to 550 nm, and red (photoconverted) Dendra2 was excited at 552 nm and collected at 580 to 650 nm.

A transmitted-light photomultiplier tube (PMT) reference image was acquired from each slice to allow identification and registering of the same slice area for longitudinal imaging. 16-bit stacks were acquired at 512 × 512 pixels (approximately 0.91 µm/pixel, zoom 1, 400 Hz, no averaging) with a 1 µm z-step over 20 optical planes. Laser power, gain, pinhole, offset and pixel size were consistent between groups and timepoints. Gain and laser power were set using the LAS X range indicator so that signal occupied approximately 30 to 60% of the intensity range without saturation. On imaging day 0 (14 DIV) a pre-photoconversion stack was acquired. The field was photoconverted (405 nm, 50% laser power, approximately 80 µW at the sample, 50 Hz, two repeats), and a post-conversion stack was taken immediately as the t = 0 baseline reading. Photoconversion power was measured at the objective using a Thorlabs S170C sensor and PM100D meter. The same field was imaged under identical settings at 3, 5, 7, 14 and 21 days after photoconversion.

Image series were exported to OME-TIFF (Bio-Formats) and processed using a custom MATLAB pipeline (https://github.com/WittonLab/dendra2_Analysis/). Stacks from the same day were registered between z-planes and across days in XY planes using a discrete Fourier transform subpixel registration on the green channel, allowing the same tissue volume to be compared at every timepoint[75]. Alignment in the Z plane across days used operator-defined ROI intensity profiles, and stacks were cropped to a common registered volume of identical dimensions.

Dendra2 tau turnover analysis

To quantify tau turnover, the mean pixel intensity was first computed across the registered volume for each channel. The normalised change in fluorescence intensity over time for each channel was calculated using the formula $\Delta F/F_0 = (F - F_0)/F_0$ where F is current fluorescence, F_0 is baseline fluorescence and ΔF is the change in fluorescence. For GFP fluorescence, baseline fluorescence was calculated from the pre-photoconversion stack on day-0 stack, whereas for RFP fluorescence the immediate post-photoconversion stack was used, so that both baselines were zero. To examine tau turnover, the proportion of red fluorescence remaining as a proportion of baseline fluorescence was calculated (F/F_0).

To account for the residual fraction of Dendra2-labelled tau retained over the course of imaging, an exponential decay to a non-zero plateau was employed by using the equation f(t) = (1 − P)·e^(−Kt) + P. t is days since photoconversion (t=0 being the post-conversion baseline fluorescence), P is the proportion of the photoconverted pool that persists, (1 − P) is the proportion of fluorescence lost relative to total fluorescence, and K is the rate of fluorescence loss per day; a larger K corresponding to faster tau turnover. K was calculated on a log scale

and P on a logit scale, constraining K > 0 and 0 < P < 1. The post-conversion baseline defines f(0) = 1 by construction and was excluded. N = 6 slices from three independent mice were analysed per experimental group.

The effect of HSPB1 expression in astrocytes on tau turnover was determined using a tau turnover rate ratio, K(GFAP-HSPB1)/K(GFAP-Control) for WT-Tau-Dendra2 and P301L/S320F-Dendra2. A ratio of 1 indicates no difference in turnover rate and a ratio above 1 indicates faster clearance. To control for group effects on log K, the ratio was obtained by exponentiating the difference between two log K values.

Tau half-life

Tau half-life (t½) was calculated as t½ = ln2/K where ln2 is the natural logarithm of 2, and K is the rate of fluorescence loss per day, and shows the time taken for the pool of tau fluorescence that is lost to fall by half. Confidence intervals for the t½ calculations were back-transformed to the original scale and therefore the interval is asymmetric.

Cumulative fluorescence change

Total cumulative fluorescence change over time was measured as area under the curve (AUC). This is calculated by trapezoidal integration of $\Delta F/F_0$ trace for each slice from day 0 to day 21, separately for the red (RFP) and green (GFP) fluorescence relative to their own baseline. $\Delta F/F_0$ is zero at baseline and becomes negative as signal declines. Increasing negative values indicate a greater cumulative loss of fluorescence relative to the pre-conversion reference baseline. For RFP photoconverted htau this reflects cumulative loss of the photoconverted pool of tau. GFP signal decreases at photoconversion and then recovers as new unconverted htau is synthesized and therefore a decrease in negative AUC values indicates greater cumulative recovery of this tau pool.

Mouse primary glial cultures

Primary mixed glial cultures were prepared from the cortex of a pool of wild-type CD1 mice on postnatal days 1 to 3, as previously described [17]. Briefly, brains were harvested and placed in ice-cold Dulbecco's modified Eagle's medium (DMEM), meninges were removed, and cerebral cortices were dissected, pooled together, and mechanically dissociated. Glial cells were grown in DMEM (Gibco, 21969-035) supplemented with 2 mM GlutaMAX (Gibco, 35050061), penicillin (100 U/ml), streptomycin (100 µg/ml; Gibco, 15140122), and 10% fetal bovine serum (FBS) (Gibco, 10500064), in poly-D-lysine (PDL; 50 µg/ml; Sigma-Aldrich, P6407)–treated flasks. To prepare astrocyte cultures, 14 to 28 DIV mixed glial cultures were

shaken at 220 rpm overnight to remove microglia. Astrocyte-enriched cultures were trypsinized in TrypLE (Gibco, 12605010) and seeded in PDL-coated plates for 3 days until they reached 80 to 90% confluency.

Astrocyte medium containing EGFP-hHSPB1 was generated as described[17]. Astrocytes were transfected with pEGFP-hsp27 wt FL (a gift from Andrea Doseff, Addgene no 17444), or an empty vector (pEGFP) for 24 h in DMEM with 10% FBS, followed by Neurobasal medium supplemented with 2% B27, GlutaMAX, penicillin (100 U/ml), and streptomycin (100 µg/ml). After 24 h, astrocyte conditioned media was then collected for treatment, and lysates were harvested to confirm the construct expression.

Mouse primary neuron cultures

Primary mouse neurons were prepared from the cortex of wild-type CD1embryos on E16.5 as previously described[17]. Briefly, brains were harvested and placed in ice-cold Hanks' balanced salt solution with HEPES, where the meninges were removed, and cerebral cortices were dissected and mechanically homogenised. Cells were cultured in poly-D-lysine (Sigma-Aldrich, P7280)-coated plates and grown in Neurobasal medium (Gibco, 21103049) supplemented with 2% B27 (Gibco, 17504044), GlutaMAX (Gibco, 35050061), penicillin (100 U/ml), and streptomycin (100 µg/ml; Gibco, 15140122) at 37°C in a humidified incubator with 5% CO2 until 12 DIV.

Neurons at 6 DIV were transduced with AAVs to express WT-htau-EGFP or mutant P301L/S320F-htau-EGFP at 2.5 × 10^{10} VGs/ml. To assess tau inclusions upon LLOMe-induced lysosomal damage, primary neurons expressing WT or mutant htau-EGFP were treated with 500 µM of LLOMe or vehicle (DMSO) for 6 h and fixed. To assess HSPB1-mediated effects on tau levels and phosphorylation, primary neurons were treated with 50 ng/ml rhHSPB1 at 6, 8 and 10 DIV prior to harvesting at 12 DIV. For SIMOA and SiMPull analysis, neurons were harvested at 8, 10 and 12 DIV in lysis buffer containing 50 mM Tris-HCl, 150 mM NaCl, 1% Triton X-100, and 5 mM EDTA followed by centrifugation at 10,000 g for 5 min at 4ºC.

For rhHSPB1-OG and Bafilomycin treatment, at 11 DIV, neurons were treated with 1.4 µg/mL HSPB1-OG for 24 h. At 12 DIV neurons were treated with 400 nM Bafilomycin A1 (Alfa Aesar, J61835.M^) or vehicle (DMSO) for 8 h. Prior to imaging, neurons were treated with 0.1 µM LysoTracker™ Red DND-99 (Invitrogen™, Thermo Fisher Scientific) and nuclei were stained with Hoechst 33342 and imaged live.

For endocytosis inhibition, neurons at 12 DIV were pre-treated with either 80 µM Dynasore (Millipore, 324410) or 20 µM Chlorpromazine hydrochloride (CPZ) (Sigma, C8138) or with vehicle DMSO or H_2O, respectively for 30 min. To inhibit macropinocytosis, neurons were pre-treated with 2 µM Latrunculin A (LatA) (Cambridge Bioscience, CAY10010630) or 20 µM 5-(N-Ethyl-N-isopropyl) amiloride (EIPA) (Bio-Techne, 3378/10) or the with vehicle ethanol or DMSO, respectively, for 30 min. Following pre-treatments with endocytosis or macropinocytosis inhibitors, neurons were then incubated with 1.4 µg/mL HSPB1-OG for 1 h. Nuclei were then stained with Hoechst 33342 and neurons imaged live.

For treatment with astrocyte-conditioned medium containing EGFP-hHSPB1, 40% of neuronal medium was replaced with medium from astrocytes grown in Neurobasal medium for 24 h prior to fixing.

SH-SY5Y cells

SH-SY5Y cells (ECACC, 94030304) were cultured in DMEM (Gibco) supplemented with 10 % FBS, 100 U/mL penicillin and 100 µg/mL streptomycin in T175 flasks and maintained at 37 ºC and 5 % CO_2. At 90 % confluency, cells were trypsinised in 0.25% trypsin/EDTA (Gibco, 25200072) and seeded into 12-well and 6-plates at $1x10^5$ or $3x10^5$ cells/well or in black/clear flat bottom 96-well plates at $1x10^4$ cells/well. Culture medium was replaced by fresh supplemented medium 24 h after seeding and prior to transfection.

SH-SY5Y cell transfection

Constructs were kindly provided by the following researchers through Addgene: mRFP-Rab5, mRFP-Rab7 (Ari Helenius (Addgene no. 14437 and 14336), LAMP1-mCherry (Amy Palmer (Addgene no. 45147), mCherry-Gal3 (Hemmo Meyer (Addgene no. 85662), mCherry-hLC3B (David Rubinsztein (Addgene no. 40827), mCherry-p62-Silent_Mutation_WT (Sascha Martens (Addgene no. 187986), and EGFP-htau wt and EGFP-htau(P301L) (Karen Ashe (Addgene no. 46904 and Addgene no. 46908). Transfection was performed using Mirus (MIR 2300) or Lipofectamine 2000 according to manufacturer's instructions using a ratio of 3 µL of Mirus or Lipofectamine 2000 per 1 µg of DNA for SH-SY5Y cells; and 1 µL of Lipofectamine 2000 per 1 µg of DNA for primary astrocytes. These were diluted in Opti-MEM (Gibco) and incubated for 20 min at room temperature allowing the DNA-lipid complexes to form. Medium was replaced with fresh complete DMEM 24 h post-transfection for Mirus or 4 h post-transfection for Lipofectamine. Cells were either live-imaged, fixed, or harvested 48 h post-transfection, as indicated for each experiment.

SH-SY5Y cell treatments

For characterization of HSPB1 internalization, SH-SY5Y cells transfected with mRFP-Rab5 or mRFP-Rab7 were treated with 1.4 µg/mL rhHSPB1-OG or OG for 1h and imaged live.

To assess the effects of HSPB1 on lysosomal damage, cells were pre-treated with 50 ng/mL of rhHSPB1 or vehicle (0.1% BSA) for 1 h, followed by treatment with 50 µM LLOMe or DMSO (vehicle) for an additional 1 h. LysoTracker (0.1 µM) was added immediately prior to live imaging. Similarly, mCherry-Galectin3, Lamp1-mCherry, mCherry-LC3 or mCherry-p62-transfected SH-SY5Y cells were treated with 50 ng/mL of rhHSPB1 or vehicle (0.1% BSA) for 1 h, followed by 50 µM or 250 µM LLOMe, as indicated, or DMSO (vehicle) for another 1 h. Cells were either live imaged or fixed.

To assess the effects of HSPB1 on tau degradation, SH-SY5Y cells transfected with EGFP WT-htau or EGFP-htau(P301L) were simultaneously treated with 50ng/ml of rhHSPB1 or vehicle (0.1% BSA) and 50 µg/ml of cycloheximide (Cambridge Bioscience, C001) to inhibit protein synthesis. Cells were harvested at 0, 3, 6, 9, 12 and 24 h post-treatment.

Imaging of live and fixed culture cells

Primary mouse neurons were fixed in 4% (w/v) paraformaldehyde (PFA; Avantor, 43368.9M) and 7.5 % sucrose for 10 min at room temperature and permeabilised with 0.1% Triton X-100 in PBS for 5 min followed by blocking in 5% (w/v) BSA (Sigma-Aldrich, A7906) and incubation with the following antibodies overnight at 4ºC: Galectin 3 (1:100, BioLegend, 125401), MAP2 (1:500, GeneTex GTX82661). Secondary anti-mouse or anti-rabbit antibodies conjugated to Alexa Fluor 488 or 568 (ThermoFisher) or anti-goat conjugated to Alexa 647 (Abcam, ab150175) at 1:1,000 and cells were incubated with Hoechst (0.1ug/ml, Invitrogen, 3342). Imaging of live neurons at 37ºC and 5% CO_2 or fixed cells was performed in an automated confocal Opera Phenix High-Content Screening system (PerkinElmer) using a 40x water immersion objective with excitation lasers 375, 488 and 561 and emission filters 435-480, 500-550 and 570-630 respectively, and creating Z-stack images. The proportion of EGFP-positive neurons that contained mutant tau aggregates was counted visually using a Zeiss Axioscope-Apotome microscope. Samples were blinded, and a minimum of 500 cells was counted per replicate, with three technical replicates per experiment.

SH-SY5Y cells were either fixed in 4% PFA (w/v) followed by nuclei staining with Hoechst, or live imaged in a confocal Opera Phenix High-Content Screening system (PerkinElmer) using a 40x or 63x water immersion objective with excitation lasers 375, 488 and 561 and emission filters 435-480, 500-550 and 570-630 respectively, and creating Z-stack images.

High-content image analysis

Harmony high-content analysis software (PerkinElmer) was used to determine the number of puncta per cell using the Find Spots building block. Parameters were calculated per live nuclei using the Find Nuclei tool or per transfected cell using the Find Cells tool, as appropriate, and averaged to total number of cells selected per well. To determine fluorophore co-localization, an empirically defined intensity threshold was applied to identified puncta using the Select Population building block. Puncta exceeding the threshold were classified as positive, and the proportion of positive puncta was calculated relative to the total number of puncta detected.

Immunoprecipitation

Protein extracts from SH-SY5Y cells either transfected with mCherry-Gal3 or non-transfected were treated with 50ng/mL rhHSPB1 or 0.1% BSA for 1 h followed by 50 uM LLOMe or DMSO treatment. After collection in lysis buffer (10 mM Tris-HCl (pH 6.8), 68.5 mM NaCl, 0.5 mM EGTA, 0.5% Triton X-100, 5% glycerol, protease and phosphatase inhibitors (Roche), 350-1000 µg protein in 600 µL buffer was incubated with Gal3 antibody (1:250, BioLegend, 125402) overnight at 4°C on a rotating wheel. After incubation with Dynabeads Protein G (Invitrogen, 10003D) for 3 h at room temperature, beads were washed in cold buffer containing 20 mM Tris-HCl, pH 7.4, 2 mM $MgCl_2$, 0.5% NP-40, and protein eluted by incubation with 24 µL of 0.1 M glycine (pH 2.5) for 10 min at room temperature, followed by resuspension in Laemmli buffer.

Western blotting

The protein content of human brain homogenates was determined by BCA assay (Pierce, 23227). Protein extracts from human brain or cellular lysates were prepared in Laemmli buffer and boiled at 95 ºC for 5 min following separation using 10 or 12% SDS–polyacrylamide gel electrophoresis in a Mini-PROTEAN Tetra system (Bio-Rad) and transferred to 0.45-µm nitrocellulose membrane (Amersham Protran, 10600002) in a Mini Trans-Blot system (Bio-Rad). Following incubation in Odyssey blocking buffer (LI-COR, 927-60003) for 1 h at RT, membranes were probed with primary antibodies: human HSPB1 (Enzo, ADI-SPA-803, 1:1,000), Tau (DAKO, A0034, 1:10,000), PHF1 (kindly gifted by Peter Davies, 1:1,000), Galectin 3 (BioLegend, 125401, 1:1,000), mCherry, alpha-tubulin (Santa Cruz, sc-5286, 1:5,000), β-actin (Abcam, Ab8226, 1:5,000). Blots were washed in TBS with 0.1% Tween 20 and incubated with the appropriate IRDye 800 or 680 conjugated anti-mouse or anti-rabbit secondary antibodies (LI-COR) diluted 1:10,000. Signal was visualized using an Odyssey CLx infrared imager (LI-COR) and quantified using ImageStudio Lite (Li-COR) software.

Simoa for HT7/AT8 detection

Bead coupling. Antibody-bead conjugation was performed following the manufacturer's protocol (Quanterix) and as previously described[31]. Carboxylated magnetic beads were washed, activated with 1-ethyl-3-(3-(dimethylamino)propyl)carbodiimide (EDC, ThermoFisher, A35391) (0.3 mg/mL) for 30 min at 4 °C, and incubated with buffer-exchanged antibody (AT8, Invitrogen, MN1020; HT7, Invitrogen, MN1000) (0.2 mg/mL) for 2 h at 2–8 °C. Following incubation, beads were washed, blocked, and stored at 4 °C until use. Coupling efficiency was assessed by measuring unbound antibody in the supernatant through absorption at 280 nm.

Plate preparation. All assays were run using the 3-step assay protocol (Quanterix) as previously described[31]. Samples were diluted with Tau 2.0 sample diluent (Quanterix) and added to a 96-well plate along with ~500,000 antibody-coupled beads. Plates were incubated for 30 min at 30 °C with shaking at 800 rpm, followed by washes and incubation (10 min, 800 rpm, 30 °C) with a biotinylated detector antibody (0.3 µg/mL), and then with streptavidin-β-galactosidase (SBG; 150 pM, 10 min, 800 rpm, 30 °C). Beads were washed, dried, and processed on the Simoa SR-X platform.

Simoa processing. On the SR-X Instrument, beads were resuspended in resorufin β-D-galactopyranoside (RGP) substrate and loaded into microwell arrays on the Simoa Disc. The fraction of active wells (fON) was calculated automatically and used to calculate the average enzymes per bead (AEB) assuming Poisson statistics. Conditions exceeding fON > 0.9 were avoided to maintain digital signal detection. A sample of cell-derived hyperphosphorylated tau aggregates of known concentration was used as a standard. After obtaining the AEB values at each calibration level, a four-parameter logistic curve was fitted.

SiMPull for detection of large aggregates and fibrils

Coverslip passivation. Coverslips were prepared for SiMPull as previously described[31]. Briefly, #1.5 borosilicate glass coverslips (26 × 76 mm; VWR, Cat. No. MENZBC026076AC40) were sequentially sonicated for 10 minutes each in 18.2 MΩ·cm water, acetone, and methanol, followed by 20 minutes in 1 M KOH. After rinsing with water and methanol, coverslips were dried with nitrogen and plasma-cleaned for 15 minutes (Femto Plasma Cleaner; Diener Electronic). Coverslips were then silanized in a 3:5:100 solution of APTES (Fisher Scientific, 10677502), acetic acid, and methanol. This involved 1-minute sonication, 10 minutes static incubation, a second 1-minute sonication, and a final 10-minute incubation. Coverslips were rinsed twice with water and once with methanol, dried with nitrogen, and fitted with 50-well silicone gaskets (Grace Bio-Labs, SKU 103250). For passivation, 9 µL of a freshly prepared 100:1 mixture of SVA-PEG-OMe (110 mg/mL, Mw ~5,000; Laysan Bio) and SVA-PEG-Biotin (100 mg/mL, Mw ~5,000; Laysan Bio) was added to each well, followed by 1 µL of 1 M

$NaHCO_3$ (pH 8.5). Coverslips were incubated in a humidity chamber for 24 hours, rinsed twice with water, and dried with nitrogen. A second passivation step followed using 9 µL of methyl-PEG4-NHS ester (10 mg/mL; Thermo Fisher, 22341) and 1 µL of 1 M $NaHCO_3$. After another 24-hour incubation, coverslips were rinsed with water, dried with nitrogen, and stored desiccated at –20 °C until use.

SiMPull with DNA-PAINT. SiMPull with DNA-PAINT was performed as previously described[33]. Wells were first washed once with PBST (PBS containing 50 mM Tris base, 150 mM NaCl, pH 7.4, and 0.05% Tween-20). NeutrAvidin (10 µL of 0.2 mg/mL in PBST; Thermo Fisher, 31000) was added to each well and incubated for 10 minutes. Following this, a wash sequence was performed: two 10 µL washes with PBST, followed by one 10 µL wash with PBS containing 1% Tween-20. Biotinylated capture antibodies were diluted to 10 nM in blocking solution (1 mg/mL BSA in PBS, filtered through 0.2 µm filter) and incubated in the wells for 10 minutes. After another wash sequence, wells were blocked with blocking solution for 10 minutes, followed by a single PBST wash. Samples were then added to the wells (10 µL per well) and incubated. Lysate samples were diluted 1:25 in PBS and incubated at room temperature for 1 hour. This was followed by a wash sequence and incubation with blocking solution for 20 min. A DNA-labelled HT7 detection antibody (DBCO TEG-AAACCACCACCACCACCACCACCACCACCACCACCA, ATDBio) was added (2 nM in 0.1 mg/mL BSA in PBS) and incubated for 15 min. After a washing cycle and an additional PBS wash, 5 µL of imaging strand (1 nM, TGGTGGT-Atto655, ATDBio) was added to each well and sealed with a clean coverslip.

Total Internal reflection Fluorescence (TIRF) microscopy

Set-up. Fluorescent images were acquired using a custom-built total internal reflection fluorescence (TIRF) microscope, as previously described[33]. The setup was based on a Nikon Ti-2 Eclipse inverted microscope body, equipped with a 60×, 1.49 N.A. Apo TIRF objective and Nikon's Perfect Focus System. Excitation was provided by 638 nm (Cobolt 06-MLD-638), 561 nm (Cobolt 06-DPL-561), 488 nm (Cobolt 06-MLD-488), and 405 nm (Cobolt 06-MLD-405) lasers (all from HÜBNER). DNA imaging strand conjugated to atto655 was excited at 638 nm. Emitted fluorescence was collected through the objective, passed through a quad-band dichroic beam splitter, and filtered using the appropriate emission filters (638 nm: BLP01-635R-25×36; all from Semrock). Images were captured on an Evolve 512 EMCCD camera (Photometrics) operating in frame-transfer mode, with an electron-multiplying gain of 6.3 electrons/ADU and 250 ADU/photon. Each image was 512 x 512 pixels, where the pixel size corresponded to 107 nm in the recorded image. To minimise bias in field selection, images were acquired in a grid pattern using an automated script in Micro-Manager.

Super-resolved image analysis. Super-resolution images were analysed as previously described[34]. Super-resolution images were reconstructed using the Picasso package. After discarding the first 100 frames, localisations were identified, fitted, and corrected for microscope drift using redundant cross-correlation. Localisations with a precision ≥30 nm were excluded. Aggregate clusters were obtained using DBSCAN implemented in scikit-learn (radius = 0.3 (~35 nm), minimum density = 10). Aggregate properties including area, perimeter, and eccentricity were determined with scikit-image, while aggregate length was measured using SKAN, reporting the summed branch distance of skeletonised aggregates. Super-resolved images were rendered with the built-in Picasso functionality.

Statistical Analysis

Statistical analysis was performed using GraphPad Prism 10 or R. For quantification of Western blot data, relative protein abundance was calculated as the signal intensity relative to the loading control. To allow comparisons across blots, all blots containing human brain homogenates included the same sample and all blots were standardized to its value. For western blots of cell lysates, data were normalized by dividing each value by the summatory of all data points on the same membrane and these were consistent across membranes. Statistical analysis was done using data from biological replicates defined as independent neuronal preparations, cell passages or individual human brain cases. Normality was assessed d'Agostino and Pearson ($n > 50$) or Shapiro-Wilk ($n < 50$) normality tests. To assess differences between two independent or paired groups, unpaired or paired Student's t-test were used respectively. Comparisons of one variable across more than two groups were performed using a one-way analysis of the variance (ANOVA) followed by Dunn's multiple comparison test. Data involving two independent variables was analysed using a two-way ANOVA followed by Tukey's or Šídák multiple comparison test as indicated or a multiple t-test analysis. Data involving three independent variables was analysed using a three-way ANOVA followed by Tuckey's multiple comparison test. Simple linear regression was used to evaluate the correlation between two variables.

Analysis of Dendra-2 signal decay was carried out using the lme4, lmerTest, nlme and emmeans R packages and treating each organotypic slice culture as one replicate. Tau turnover was calculated as the rate of decay of the photoconverted red Dendra2 signal, and treatment effects were determined using a nonlinear mixed-effects model with a constrained exponential decay-to-plateau function. f(t)=(1-P)e^{-Kt}+P. (t) is time since photoconversion, (K) is the rate constant of fluorescence loss, and (P) is the fraction of photoconverted tau retained over time. RFP half-life, RFP AUC, and GFP AUC were analysed using Kruskal-Wallis omnibus test followed by pairwise comparisons with Holm adjustment for multiple

testing. Data presented as mean ± standard error of the mean (SEM), standard deviation (SD) or confidence interval, as indicated. Results were considered statistically significant when p-value < 0.05. *P<0.05, **P<0.01, ***P<0.001, ****P<0.0001.

Acknowledgements: We thank C. Troakes at the London Brain Bank for Neurodegenerative diseases, G. Chennell at the Wohl Cellular Imaging Centre at King's College London and the RILD Imaging Facility at the University of Exeter, for their support and assistance with this work. PHF-1 antibody was a gift from the late P. Davies. Illustrations were created with Biorender.com

Funding: This work was supported by a Medical Research Council Transition Support Award (MR/V036947/1) and Alzheimer's Research project grant (ARUK-MPG2024-019) to MJ-S. Part of P.B-L work was supported by Alzheimer's Research UK (ARUK-PhD2018-002) to W.N and additionally by Alzheimer's Research UK (ARUK-ECRBF2023B-005) and Alzheimer's Society Postdoctoral Fellowship (Ref. 663) to P.B-L. C.P. is funded by a BRACE Dementia Research PhD Scholarship to W.N., M.J-S and C.L.C. C.L.C was supported by a Race Against Dementia Alzheimer's Research UK fellowship (ARUK-RADF2019A-003).

Author contributions: P.B-L and F.Y. performed most of the experiments, analysis, and interpretation of the data, and contributed to study design and conceptualization; C.P., J.C.C., J.W. and W.N. performed, analyzed, interpreted and/or supervised Tau-Dendra2 assays; D.B. and D.K. performed, analyzed, interpreted and/or supervised SiMPull and Simoa assays; L.V., R.G-H, S.C-J. and S.J.P. contributed to additional experiments and/or data analysis; A.R.C. and C.L.C. provided the AAVs for htau and methodology; M.J.-S. contributed to additional experiments, study design, conceptualized the study, obtained funding, and supervised the work; P.B-L and M.J.-S. wrote the manuscript. All authors reviewed and approved the final manuscript.

Competing interests: The authors declare that they have no competing interests.

Data and materials availability: The Dendra2 analysis code can be accessed in the following GitHub repository https://github.com/WittonLab/dendra2_Analysis/. All other data needed to evaluate the conclusions in the paper are present in the paper and/or the Supplementary Materials.

Ethics declaration: not applicable

References

1. Knopman, D. S. *et al.* Alzheimer disease. *Nat Rev Dis Primers* **7**, 33 (2021).
2. Braak, H. & Braak, E. Neuropathological stageing of Alzheimer-related changes. *Acta Neuropathol* **82**, 239–259 (1991).
3. De Tito, S. & Tooze, S. A. Lysosomal homeostasis at the crossroads of neurodegeneration. *J Clin Invest* **136**, e199845 (2026).
4. Nixon, R. A. Amyloid precursor protein and endosomal-lysosomal dysfunction in Alzheimer's disease: inseparable partners in a multifactorial disease. *FASEB J* **31**, 2729–2743 (2017).
5. Pollack, S. J. *et al.* Truncated tau interferes with the autophagy and endolysosomal pathway and results in lipid accumulation. *Cell Mol Life Sci* **81**, 304 (2024).
6. Yoon, B. H. *et al.* Targeted autophagic clearance of Tau protects against Alzheimer's disease through amelioration of Tau-mediated lysosomal stress. *Theranostics* **15**, 9240–9260 (2025).
7. Mirfakhar, F. S. *et al.* A pathogenic Tau mutation drives autophagy-lysosome dysfunction that limits Tau degradation in a model of frontotemporal dementia. *Nat Commun* **17**, 2699 (2026).
8. Fleming, A. *et al.* The different autophagy degradation pathways and neurodegeneration. *Neuron* **110**, 935–966 (2022).
9. Maejima, I. *et al.* Autophagy sequesters damaged lysosomes to control lysosomal biogenesis and kidney injury. *EMBO J* **32**, 2336–2347 (2013).
10. Kravić, B. *et al.* Ubiquitin profiling of lysophagy identifies actin stabilizer CNN2 as a target of VCP/p97 and uncovers a link to HSPB1. *Mol Cell* **82**, 2633-2649.e7 (2022).

11. Gallagher, E. R. & Holzbaur, E. L. F. The selective autophagy adaptor p62/SQSTM1 forms phase condensates regulated by HSP27 that facilitate the clearance of damaged lysosomes via lysophagy. *Cell Rep* **42**, 112037 (2023).
12. Haslbeck, M., Weinkauf, S. & Buchner, J. Small heat shock proteins: Simplicity meets complexity. *J Biol Chem* **294**, 2121–2132 (2019).
13. Vendredy, L., Adriaenssens, E. & Timmerman, V. Small heat shock proteins in neurodegenerative diseases. *Cell Stress Chaperones* https://doi.org/10.1007/s12192-020-01101-4 (2020) doi:10.1007/s12192-020-01101-4.
14. Abisambra, J. F. *et al.* Phosphorylation dynamics regulate Hsp27-mediated rescue of neuronal plasticity deficits in tau transgenic mice. *J. Neurosci.* **30**, 15374–15382 (2010).
15. Freilich, R. *et al.* Competing protein-protein interactions regulate binding of Hsp27 to its client protein tau. *Nat Commun* **9**, 4563 (2018).
16. Baughman, H. E. R., Pham, T.-H. T., Adams, C. S., Nath, A. & Klevit, R. E. Release of a disordered domain enhances HspB1 chaperone activity toward tau. *Proc Natl Acad Sci U S A* **117**, 2923–2929 (2020).
17. Yang, F. *et al.* Reactive astrocytes secrete the chaperone HSPB1 to mediate neuroprotection. *Sci Adv* **10**, eadk9884 (2024).
18. Escartin, C. *et al.* Reactive astrocyte nomenclature, definitions, and future directions. *Nat Neurosci* **24**, 312–325 (2021).
19. Matafora, V. *et al.* Proteomics of the astrocyte secretome reveals changes in their response to soluble oligomeric Aβ. *J Neurochem* https://doi.org/10.1111/jnc.15875 (2023) doi:10.1111/jnc.15875.
20. Askenazi, M. *et al.* Compilation of reported protein changes in the brain in Alzheimer's disease. *Nat Commun* **14**, 4466 (2023).

21. Thuringer, D. & Garrido, C. Molecular chaperones in the brain endothelial barrier: neurotoxicity or neuroprotection? *FASEB J* **33**, 11629–11639 (2019).
22. Croft, C. L. *et al.* rAAV-based brain slice culture models of Alzheimer's and Parkinson's disease inclusion pathologies. *J. Exp. Med.* **216**, 539–555 (2019).
23. Beltran-Lobo, P. *et al.* P2X7R influences tau aggregate burden in human tauopathies and shows distinct signalling in microglia and astrocytes. *Brain Behav Immun* **114**, 414–429 (2023).
24. Macia, E. *et al.* Dynasore, a cell-permeable inhibitor of dynamin. *Dev Cell* **10**, 839–850 (2006).
25. Daniel, J. A. *et al.* Phenothiazine-derived antipsychotic drugs inhibit dynamin and clathrin-mediated endocytosis. *Traffic* **16**, 635–654 (2015).
26. Koivusalo, M. *et al.* Amiloride inhibits macropinocytosis by lowering submembranous pH and preventing Rac1 and Cdc42 signaling. *J Cell Biol* **188**, 547–563 (2010).
27. Coué, M., Brenner, S. L., Spector, I. & Korn, E. D. Inhibition of actin polymerization by latrunculin A. *FEBS Lett* **213**, 316–318 (1987).
28. Yoshimori, T., Yamamoto, A., Moriyama, Y., Futai, M. & Tashiro, Y. Bafilomycin A1, a specific inhibitor of vacuolar-type H(+)-ATPase, inhibits acidification and protein degradation in lysosomes of cultured cells. *J Biol Chem* **266**, 17707–17712 (1991).
29. Jia, J. *et al.* Galectin-3 Coordinates a Cellular System for Lysosomal Repair and Removal. *Dev Cell* **52**, 69-87.e8 (2020).
30. Eapen, V. V., Swarup, S., Hoyer, M. J., Paulo, J. A. & Harper, J. W. Quantitative proteomics reveals the selectivity of ubiquitin-binding autophagy receptors in the turnover of damaged lysosomes by lysophagy. *Elife* **10**, e72328 (2021).

31. Böken, D. *et al.* Profiling Protein Aggregate Size Using Single-Molecule Array Technology. *Anal Chem* https://doi.org/10.1021/acs.analchem.6c03315 (2026) doi:10.1021/acs.analchem.6c03315.
32. Böken, D. *et al.* Temporal Trajectories of the Tau Aggregate Interactome Reveal Stage-Specific Vulnerabilities in Alzheimer's Disease. *Adv Sci (Weinh)* e77822 (2026) doi:10.1002/advs.77822.
33. Böken, D. *et al.* Single-Molecule Characterization and Super-Resolution Imaging of Alzheimer's Disease-Relevant Tau Aggregates in Human Samples. *Angew Chem Int Ed Engl* **63**, e202317756 (2024).
34. Böken, D. *et al.* Nanoscopic tau aggregates are not shared intermediates but disease-specific entities across tauopathies. *Cell Rep* **45**, 116934 (2026).
35. Croft, C. L. *et al.* Photodynamic studies reveal rapid formation and appreciable turnover of tau inclusions. *Acta Neuropathol* **141**, 359–381 (2021).
36. Hipp, M. S., Kasturi, P. & Hartl, F. U. The proteostasis network and its decline in ageing. *Nat Rev Mol Cell Biol* **20**, 421–435 (2019).
37. Hetz, C. Adapting the proteostasis capacity to sustain brain healthspan. *Cell* **184**, 1545–1560 (2021).
38. Brehme, M. *et al.* A chaperome subnetwork safeguards proteostasis in aging and neurodegenerative disease. *Cell Rep* **9**, 1135–1150 (2014).
39. Mathys, H. *et al.* Single-cell transcriptomic analysis of Alzheimer's disease. *Nature* **570**, 332–337 (2019).
40. Grubman, A. *et al.* A single-cell atlas of entorhinal cortex from individuals with Alzheimer's disease reveals cell-type-specific gene expression regulation. *Nat. Neurosci.* **22**, 2087–2097 (2019).

990 41. Leng, K. *et al.* Molecular characterization of selectively vulnerable neurons in
991 Alzheimer's disease. *Nat Neurosci* **24**, 276–287 (2021).
992 42. Smith, A. M. *et al.* Diverse human astrocyte and microglial transcriptional responses to
993 Alzheimer's pathology. *Acta Neuropathol* **143**, 75–91 (2022).
994 43. Serrano-Pozo, A. *et al.* Astrocyte transcriptomic changes along the spatiotemporal
995 progression of Alzheimer's disease. *Nat Neurosci* **27**, 2384–2400 (2024).
996 44. Tytell, M., Greenberg, S. G. & Lasek, R. J. Heat shock-like protein is transferred from
997 glia to axon. *Brain Res.* **363**, 161–164 (1986).
998 45. Oliveira, A. O., Osmand, A., Outeiro, T. F., Muchowski, P. J. & Finkbeiner, S. αB-
999 Crystallin overexpression in astrocytes modulates the phenotype of the BACHD mouse
1000 model of Huntington's disease. *Hum Mol Genet* **25**, 1677–1689 (2016).
1001 46. Bason, M. *et al.* Astrocytic expression of the chaperone DNAJB6 results in non-cell
1002 autonomous protection in Huntington's disease. *Neurobiol Dis* **124**, 108–117 (2019).
1003 47. Abjean, L. *et al.* Reactive astrocytes promote proteostasis in Huntington's disease
1004 through the JAK2-STAT3 pathway. *Brain* **146**, 149–166 (2023).
1005 48. Heilman, P. L. *et al.* HSPB1 mutations causing hereditary neuropathy in humans disrupt
1006 non-cell autonomous protection of motor neurons. *Exp Neurol* **297**, 101–109 (2017).
1007 49. Wu, J. *et al.* Heat shock proteins function as signaling molecules to mediate neuron-glia
1008 communication in C. elegans during aging. *Nat Neurosci* **28**, 1635–1648 (2025).
1009 50. Chaplot, K., Jarvela, T. S. & Lindberg, I. Secreted Chaperones in Neurodegeneration.
1010 *Front Aging Neurosci* **12**, 268 (2020).
1011 51. Holmes, B. B. *et al.* Heparan sulfate proteoglycans mediate internalization and
1012 propagation of specific proteopathic seeds. *Proc Natl Acad Sci U S A* **110**, E3138-3147
1013 (2013).

52. Wu, J. W. *et al.* Small misfolded Tau species are internalized via bulk endocytosis and anterogradely and retrogradely transported in neurons. *J Biol Chem* **288**, 1856–1870 (2013).
53. Falcon, B. *et al.* Conformation determines the seeding potencies of native and recombinant Tau aggregates. *J Biol Chem* **290**, 1049–1065 (2015).
54. Evans, L. D. *et al.* Extracellular Monomeric and Aggregated Tau Efficiently Enter Human Neurons through Overlapping but Distinct Pathways. *Cell Rep* **22**, 3612–3624 (2018).
55. Shimura, H., Miura-Shimura, Y. & Kosik, K. S. Binding of tau to heat shock protein 27 leads to decreased concentration of hyperphosphorylated tau and enhanced cell survival. *J Biol Chem* **279**, 17957–17962 (2004).
56. Zhang, S. *et al.* Specific binding of Hsp27 and phosphorylated Tau mitigates abnormal Tau aggregation-induced pathology. *Elife* **11**, e79898 (2022).
57. Baughman, H. E. R., Clouser, A. F., Klevit, R. E. & Nath, A. HspB1 and Hsc70 chaperones engage distinct tau species and have different inhibitory effects on amyloid formation. *J. Biol. Chem.* https://doi.org/10.1074/jbc.M117.803411 (2018) doi:10.1074/jbc.M117.803411.
58. Flavin, W. P. *et al.* Endocytic vesicle rupture is a conserved mechanism of cellular invasion by amyloid proteins. *Acta Neuropathol* **134**, 629–653 (2017).
59. Falcon, B., Noad, J., McMahon, H., Randow, F. & Goedert, M. Galectin-8-mediated selective autophagy protects against seeded tau aggregation. *J Biol Chem* **293**, 2438–2451 (2018).
60. Wang, Y. *et al.* Tau fragmentation, aggregation and clearance: the dual role of lysosomal processing. *Hum. Mol. Genet* **18**, 4153–4170 (2009).

61. Krüger, U., Wang, Y., Kumar, S. & Mandelkow, E.-M. Autophagic degradation of tau in primary neurons and its enhancement by trehalose. *Neurobiol. Aging* **33**, 2291–2305 (2012).

62. Schaeffer, V. *et al.* Stimulation of autophagy reduces neurodegeneration in a mouse model of human tauopathy. *Brain* **135**, 2169–2177 (2012).

63. Ozcelik, S. *et al.* Rapamycin attenuates the progression of tau pathology in P301S tau transgenic mice. *PLoS ONE* **8**, e62459 (2013).

64. Polito, V. A. *et al.* Selective clearance of aberrant tau proteins and rescue of neurotoxicity by transcription factor EB. *EMBO Mol Med* **6**, 1142–1160 (2014).

65. Lopez, A. *et al.* A152T tau allele causes neurodegeneration that can be ameliorated in a zebrafish model by autophagy induction. *Brain* **140**, 1128–1146 (2017).

66. Caballero, B. *et al.* Interplay of pathogenic forms of human tau with different autophagic pathways. *Aging Cell* **17**, (2018).

67. Caballero, B. *et al.* Acetylated tau inhibits chaperone-mediated autophagy and promotes tau pathology propagation in mice. *Nat Commun* **12**, 2238 (2021).

68. Silva, M. C. *et al.* Prolonged tau clearance and stress vulnerability rescue by pharmacological activation of autophagy in tauopathy neurons. *Nat Commun* **11**, 3258 (2020).

69. Thurston, T. L. M., Wandel, M. P., von Muhlinen, N., Foeglein, A. & Randow, F. Galectin 8 targets damaged vesicles for autophagy to defend cells against bacterial invasion. *Nature* **482**, 414–418 (2012).

70. Hung, Y.-H., Chen, L. M.-W., Yang, J.-Y. & Yang, W. Y. Spatiotemporally controlled induction of autophagy-mediated lysosome turnover. *Nat Commun* **4**, 2111 (2013).

71. Koerver, L. *et al.* The ubiquitin-conjugating enzyme UBE2QL1 coordinates lysophagy in response to endolysosomal damage. *EMBO Rep* **20**, e48014 (2019).
72. Flavin, W. P. *et al.* Endocytic vesicle rupture is a conserved mechanism of cellular invasion by amyloid proteins. *Acta Neuropathol* **134**, 629–653 (2017).
73. Kakuda, K. *et al.* Lysophagy protects against propagation of α-synuclein aggregation through ruptured lysosomal vesicles. *Proc Natl Acad Sci U S A* **121**, e2312306120 (2024).
74. Zhong, W. *et al.* Lysosomal escape and TMEM106B fibrillar core determine TDP-43 seeding outcomes. *bioRxiv* 2025.12.19.695531 (2025) doi:10.64898/2025.12.19.695531.
75. Guizar-Sicairos, M., Thurman, S. T. & Fienup, J. R. Efficient subpixel image registration algorithms. *Opt Lett* **33**, 156–158 (2008).

Figure legends

Figure 1. HSPB1 increases in AD brain and localizes predominantly to astrocytes with post-transcriptional neuronal accumulation. A. Representative immunoblots of human HSPB1 in control (Braak 0-II), moderate (Braak III-IV) and severe (Braak V-VI) AD samples in Brodman Areas 9 (BA9) and BA21. β-actin was used as loading control. **B-C**. Bar graphs display the quantification of HSPB1 protein levels normalised to β-actin as a percentage of average control (Braak 0-II) in (**B)** BA9 and (**C)** BA21. Data is mean ± standard deviation (SD). BA9: N=10 per group (Braak 0-II, III-IV, V-VI). BA21: N=4 (Braak 0-II), N=5 (Braak III-IV), N=4 (Braak V-VI). One-way ANOVA with Dunn's multiple comparisons. **D.** Representative images of HSPB1 (green), ALDH1L1 (magenta) or MAP2 (magenta) in control (Braak 0-II) and AD (Braak V-VI) cases. Scale bar: 50 μm. Vascular structures excluded from the analysis are indicated with an arrowhead. Insets indicate areas of colocalization displayed at higher magnification in (F, H). **E.** Bar chart shows the percentage of HSPB1-positive cells that are either ALDH1L1+ astrocytes or MAP2+ neurons in control (Braak 0-II) or AD (Braak V-VI)

cases. N=5. Data is mean ± SD. Two-way ANOVA with Šídák multiple comparison test. **F-I.** Representative images of HSPB1+ (green) and ALDH1L1+ astrocytes **(F)** or **(H)** MAP2+ neurons in control (Braak 0-II) and AD (Braak V-VI) cases. Bar charts display the quantification of HSPB1 signal intensity in **(G)** astrocytes or **(I)** neurons. N=5. Data is mean ± SD. Unpaired t-test. **J.** Representative images of *HSPB1* mRNA (magenta) and ALDH1L1+ or MAP2+ (green) cells in control (Braak 0-III) and AD (Braak V-VI) brain. DAPI is used as nuclei stain. Examples of cells containing *HSPB1* mRNA are indicated with arrowheads. Scale bar: 20 µm. **K-L.** Bar graphs display the number of **(K)** astrocytes or **(L)** neurons containing *HSPB1* mRNA in control (Braak 0-III) and severe AD (Braak V-VI) brain. N=5. Data is mean ± SD. Unpaired t-test. **M.** Schematic represents organotypic brain slices transduced with AAV-GFAP-hHSPB1. **N.** Representative images of human HSPB1 (green) and GFAP or MAP2 (magenta). Arrowheads indicate HSPB1+ astrocytes and neurons *ex vivo*. Scale bar: 50 µm. **P*<0.05, ***P*<0.01.

Figure 2. Astrocytic HSPB1 associates with hallmarks of neuronal tau pathology in AD. **A.** Schematic represents organotypic brain slices transduced with AAVs to express WT htau-EGFP or mutant P301L/S320F-htau-EGFP and simultaneously transduced with AAV-GFAP or AAV-GFAP-hHSPB1. **B.** Representative immunoblots of phosphorylated tau (PHF1, Ser396/Ser404), total tau and HSPB1 in total, soluble and sarkosyl-insoluble tau fractions. **C.** Bar graph displays the levels of HSPB1 in the tau sarkosyl insoluble fraction relative to total tau in lysates of organotypic slices transduced with WT htau or mutant P301L/S320F-htau. N=3. Data is mean ± SD. Unpaired t-test. **D.** Representative immunoblots of total, soluble and sarkosyl-insoluble tau fractions of BA9 AD brain (Braak III-VI) immunoblotted with antibodies against PHF1, total tau and HSPB1. **E-F.** Bar graphs show the correlation between the levels of **(E)** soluble HSPB1 and soluble tau and **(F)** insoluble HSPB1 and insoluble PHF1 phospho tau. Colours represent Braak III (dark blue), IV (light blue), Braak V (light purple) and Braak VI (dark purple) (N=24). Simple linear regression. **G.** Representative images of areas with no lesions (NL) or dystrophic neurites (DNs) in AD brain (Braak V-VI) sections immunolabelled with antibodies against AT8 (blue), HSPB1 (green) and GFAP (magenta). Scale bar: 25 µm. **H-J.** Violin plots display the **(H)** integrated density of GFAP, and the Pearson's correlation coefficient between **(I)** HSPB1 and GFAP or HSPB1 and AT8 **(J)**. N=5. Each data point represents the mean Pearson's *R* value per tissue. Forty lesions were analysed per case. Dotted lines indicate the median and quartiles. Paired t-test. **K.** Representative images of AD brain (Braak V-VI) sections immunolabelled with antibodies against HSPB1 (green) and AT8 (magenta) and MAP2 (blue). Scale bar: 50 µm. Neurons with AT8-positive neurofibrillary

tangles (NFTs) are indicated with an arrowhead. Inset indicates HSPB1-positive NFTs and is displayed at higher magnification. Scale bar: 25 μm. **L-M.** Bar graph displays the percentages of **(L)** MAP2-positive neurons that are AT8-positive and **(M)** AT8-positive NFTs that are HSPB1-positive. Data is mean ± SD. *P<0.05, **P<0.01, ***P<0.001.

Figure 3. HSPB1 is internalized and targeted to lysosomes by macropinocytosis. A. Representative images of SH-SY5Y cells transfected with Rab5-mRFP (magenta) and treated with rhHSPB1-OG (green). Nuclei are stained with Hoechst 33342. Scale bar: 25 μm. Bar graph displays the **(B)** number of Rab5+, HSPB1+ and double positive HSPB1+ and Rab5+ puncta per transfected cell and the **(C)** percentage of double HSPB1+Rab5+ puncta relative to the number of HSPB1 puncta per cell. Dotted line indicates the mean, and its value is displayed above each variable. N=3. **D.** Representative images of SH-SY5Y cells transfected with Rab7-mRFP (magenta) and treated with rhHSPB1-OG (green). Nuclei are stained with Hoechst 33342. Scale bar: 25 μm. Bar graph displays the **(E)** number of Rab7+, HSPB1+ and double positive HSPB1+ and Rab7+ puncta per transfected cell and the **(F)** percentage of double HSPB1+ and Rab7+ puncta relative to the number of HSPB1 puncta per cell. N=3. **G-J.** Representative images of neurons treated with **(G)** Dynasore (80 μM) and Chlorpromazine (CPZ, 20 μM) or **(I)** EIPA (20 μM) or Latrunculin A (LatA, 2 μM) for 30 min and their corresponding vehicles prior to adding rhHSPB1-OG for 1 h and live imaging. Scale bar: 50 μm. Insets marked with a white rectangle are displayed below at higher magnification. Dotted line indicates the outline of the cell. Arrows indicate HSPB1-OG+ puncta. Scale bar: 10 μm. Bar graphs show the quantification of the average number of rhHSPB1-OG+ puncta per cell in neurons treated with **(H)** clathrin-mediated inhibitors or **(J)** macropinocytosis inhibitors. N=5. Data is mean ± SD. One-way ANOVA with Tukey multiple comparisons. **K.** Representative images of primary mouse neurons at 12 DIV pre-treated with rhHSPB1-OG (green) for 24 h and treated with 400 nM Bafilomycin or vehicle (DMSO) for the last 8 h. Functional lysosomes are stained with LysoTracker (magenta) and nuclei with Hoechst 33342. Scale bar: 50 μm. White insets define cells displayed at higher magnification. Scale bars 10 μm. **L.** Bar graph displays the average number of rhHSPB1-OG+ puncta per neuron. N=3. Data is mean ± SD. Unpaired t-test. **P<0.01, ***P<0.001.

Figure 4. Internalized HSPB1 is recruited to damaged lysosomes and restores lysosomal integrity. A. Representative images of SH-SY5Y cells pre-treated with 50 ng/mL rhHSPB1 or vehicle (0.1 % BSA) for 1 h and incubated with 250 μM LLOMe or vehicle (DMSO)

for another 1 h. Functional lysosomes are imaged live with LysoTracker (magenta) and nuclei with Hoechst 33342. Scale bar: 50 µm. **B.** Bar graph displays the quantification of average number of LysotTacker puncta per cell. Scale bar: 50 µm. N=3. Data is mean ± SD. Multiple unpaired t-test. **C.** Representative images of live imaged SH-SY5Y cells expressing mCherry-Galectin3 (mCherry-Gal3, magenta), pre-treated with 50 ng/mL rhHSPB1 for 1 h and treated with 50 µM LLOMe or vehicle for another 1h. Scale bar: 50 µm. Arrowheads indicate mCherry-Gal3 puncta. **D.** Bar graph displays the average number mCherry-Gal3 puncta per transfected cell. N=3. Data is mean ± SD. Multiple unpaired t-test. **E.** Representative images of SH-SY5Y cells expressing LAMP1-mCherry (magenta) pre-treated with 50 ng/mL rhHSPB1 or vehicle (0.1 % BSA) for 1 h and incubated with 250 µM LLOMe or vehicle (DMSO) for 1 h. Nuclei are stained with Hoechst 33342. Scale bar: 50 µm. **F.** Bar graph displays the average number of LAMP1-mCherry puncta per transfected cell. N=3. Data is mean ± SD. Multiple unpaired t-test. **G.** Representative images of SH-SY5Y cells expressing mCherry-Gal3 (magenta), incubated with rhHSPB1-OG (green) for 1 h prior to treatment with 50 µM LLOMe or vehicle for 1 h. Nuclei are stained with Hoechst 33342. Scale bar: 50 µm. Arrowheads indicate puncta positive for both rhHSPB1-OG and mCherry-Gal3. **H.** Bar graph displays the number of double mCherry-Gal3 and HSPB1-OG positive puncta per transfected cell. N=3. Data is mean ± SD. Unpaired t-test. **I.** Representative images of SH-SY5Y cells expressing LAMP1-mCherry (magenta) and incubated with rhHSPB1-OG (green) for 1 h prior to treatment with 50 µM LLOMe or vehicle for 1 h. Nuclei are stained with Hoechst 33342. Scale bar: 25 µm. Arrowheads indicate puncta positive for both rhHSPB1-OG and LAMP1-mCherry. **J.** Bar graph displays the number of double LAMP1-mCherry and rhHSPB1-OG positive puncta per transfected cell. N=3. Data is mean ± SD. Unpaired t-test. *P<0.05, ***P<0.001.

Figure 5. Internalized HSPB1 promotes recruitment of LC3 to damaged lysosomes. A. Representative images of SH-SY5Y cells expressing mCherry-LC3 (magenta), pre-treated with rhHSPB1 or vehicle (0.1 % BSA) for 1h and incubated with 250 µM LLOMe or vehicle (DMSO) for another 1 h. Nuclei are stained with Hoechst 33342. Scale bar: 50 µm. **B.** Bar graph displays the quantification of average number of mCherry-LC3 puncta (magenta) per cell. N=3. Data is mean ± SD. Multiple paired t-test. **C.** Representative images of SH-SY5Y cells expressing mCherry-LC3 (magenta), pre-treated with rhHSPB1-OG (green) and treated with 50 µM LLOMe or vehicle. Scale bar: 50 µm. Arrowheads indicate puncta positive for rhHSPB1-OG and mCherry-LC3. **D.** Bar graph displays the average number of double mCherry-LC3 and HSPB1-OG positive puncta per transfected cell. N=3. Data is mean ± SD. Unpaired t-test. **E.** Representative images of SH-SY5Y cells expressing mCherry-p62

(magenta), pre-treated with 50 ng/mL rhHSPB1 or 0.1 % BSA for 1h and incubated with 250 μM LLOMe or vehicle for 1 h. Nuclei are stained with Hoechst 33342. Scale bar: 50 μm. **F.** Bar graph displays quantification of the average number of mCherry-p62 puncta (magenta) per cell. N=4. Data is mean ± SD. Multiple paired t-test. *P<0.05, ***P<0.001.

Figure 6. HSPB1 reduces the number of long nanoscopic tau aggregates. A. Diagram depicts the SIMOA assay for tau aggregate detection using HT7-HT7 or AT8-AT8 monoclonal antibody pairs to capture and detect soluble tau aggregates. **B-C.** Bar graphs display the concentration of aggregates detected for **(B)** HT7 total tau aggregates or **(C)** tau aggregates phosphorylated at the AT8 epitope in primary neurons expressing WT or mutant (P301L/S320F) htau, treated with 50 ng/mL rhHSPB1 or vehicle for 24 h and harvested at 8, 10 or 12 DIV. N=4. Data is mean ± SD. Three-way ANOVA followed by Tuckey multiple comparison test with (**B)** significant main effects of htau ($F(1,36) = 32.37$, $P < 0.0001$) and time ($F(2,36) = 23.03$, $P < 0.0001$), time × htau interaction ($F(2,36) = 20.77$, $P < 0.0001$) and **(C)** main effects of Time ($F(2,18) = 126$, $P < 0.0001$) and htau ($F(1,18) = 92.6$, $P < 0.0001$); time × htau interaction ($F(2,18) = 80.8$, $P < 0.0001$), time × treatment ($F(2,18) = 5.29$, $P = 0.0155$) and time × htau × treatment interaction ($F(2,18) = 4.19$, $P = 0.0320$). **D.** Diagram representing the SiMPull assay for the detection of tau aggregates detected with HT7-HT7 antibody pairs. **E-F.** Representative images of super-resolved tau aggregates from neurons expressing WT or mutant (P301L/S320F) htau and treated with rhHSPB1 or vehicle using HT7 SiMPull. Scale bar: 1 μm. White insets are displayed below **(F)** at higher magnification. Scale bar: 100 nm. **G-H.** Bar graphs display the percentage of **(G)** fibrillar aggregates (eccentricity >0.9) or **(H)** long aggregates (>150 nm length). N=4. Data is mean ± SD. Two-way ANOVA with Šídák multiple comparison test. *P<0.05.

Figure 7. Uptake of HSPB1 enhances lysosomal clearance of htau. A. Representative images of primary neurons expressing EGFP-tagged WT or mutant (P301L/S320F) human tau (htau, green) and immunolabelled for Gal3 (magenta) and MAP2 (red). Nuclei are stained with Hoechst 33342. Scale bar: 50 μm. White inset indicates a neuron expressing P301L/S320F htau with an inclusion and is displayed below at higher magnification. Scale bar: 25 μm. **B-C.** Bar graphs show the percentage of **(B)** WT and P301L/S320F htau-neurons that are immuno-positive for Gal3 or **(C)** P301L/S320F htau-neurons with and without inclusions that are immuno-positive for Gal3. N=3. Data is mean ± SD. Unpaired t-test. **D.** Representative images of primary neurons expressing EGFP-tagged mutant (P301L/S320F) htau treated with

500 μM LLOMe or vehicle for 6h. Nuclei are stained with Hoechst 33342. Arrowheads indicate neurons with htau inclusions. Scale bar: 100 μm. **E.** Bar graph displays the percentage of EGFP-P301L/S320F htau-expressing neurons harbouring tau inclusions following treatment with 500 μM LLOMe or DMSO (vehicle). N=3. Data is mean ± SD. Unpaired t-test. **F-G.** Representative immunoblots of lysates from SH-SY5Y cells transfected with EGFP-tagged **(F)** WT or **(G)** mutant (P301L) htau and treated with 50 μg/mL cycloheximide alongside 50 ng/mL rhHSPB1 or vehicle (0.1% BSA) and collected at the indicated time points. Graphs show the expression of htau-EGFP normalised to α-tubulin per sample at each time point. Shaded lines delimit the SD per treatment at each time point. N=6. Data is mean ± SD. Unpaired t-test. **P*<0.05, ***P*<0.01, ****P*<0.001.

Figure 8. Astrocytic HSPB1 accelerates mutant tau turnover *ex vivo*. A). Diagram shows the experimental design for longitudinal Dendra2 pulse-chase imaging. Organotypic brain slice cultures were co-transduced with AAV-WT-htau-Dendra2 or AAV-P301L/S320F-htau-Dendra2 and AAV-GFAP or AAV-GFAP-hHSPB1 at DIV 0. AAV-htau-Dendra2 was photoconverted using targeted 405 nm illumination at 14 DIV (0 days post-conversion) and the same field was re-imaged on days 3, 5, 7, 14 and 21 post-conversion. Representative images show green (GFP) photoconversion to red (RFP) tau. Representative tilescan image shows the area of targeted photoconversion (red) in a representative organotypic brain slice, surrounded by the unconverted field (green). Scale bars are 25 μm and 200 μm. **B-E.** Representative post-conversion images of **(B)** WT-htau-Dendra2 or **(D)** P301L/S320F-htau-Dendra2 (red) co-transduced with either AAV-GFAP or AAV-GFAP-hHSPB1 in the same field of the organotypic slice at 0, 5 and 14 DIV. Arrowheads indicate the same cell across time. Scale bar: 25 μm. Graphs display the fraction of photoconverted **(C)** WT-htau or **(E)** P301L/S320F-htau Dendra2 pool retained over 21 days. Data points represent geometric means ± SEM on the log scale. Thin lines represent data from individual slice cultures, thick lines are decay curves with 95% confidence intervals. p value is the overall effect of hHSPB1 on tau turnover. Nonlinear mixed-effects model. f(t)=(1-P)e^{-Kt}+P. (t) is time since photoconversion, (K) is the rate constant of fluorescence loss, and (P) is the fraction of photoconverted tau retained over time. N=6 organotypic slice cultures per group. **F.** Photoconverted tau turnover rate ratios for AAV-GFAP-hHSPB1 relative to AAV-GFAP in slices expressing WT-htau-Dendra2 or P301L/S320F-htau-Dendra2, with 95% confidence intervals. WT-htau-Dendra2, mean = 1.21 (95% CI: 0.76–1.93, p = 0.412); P301L/S320F-htau, mean = 1.83 (95% CI: 1.15-2.91, p = 0.022). No significant differences between WT-htau-Dendra2 or P301L/S320F-htau-Dendra2 (p = 0.21). N=6 organotypic slice cultures per group.

G. Proposed model summarizing the findings of the study. Our data support a model in which reactive astrocytes secrete HSPB1 into the extracellular space, where it is internalized by neurons harbouring pathological tau. Tau inclusions impair tau clearance and drive lysosomal damage and, in this scenario, uptake of astrocyte-derived HSPB1 promotes the recruitment of Gal3 to damaged lysosomes. Subsequent recruitment of the autophagy machinery promotes degradation of damaged lysosomes by lysophagy. This promotes lysosomal integrity, thereby facilitating tau clearance in neurons and reduced accumulation of tau inclusions. Created with BioRender.com.

Figure 1

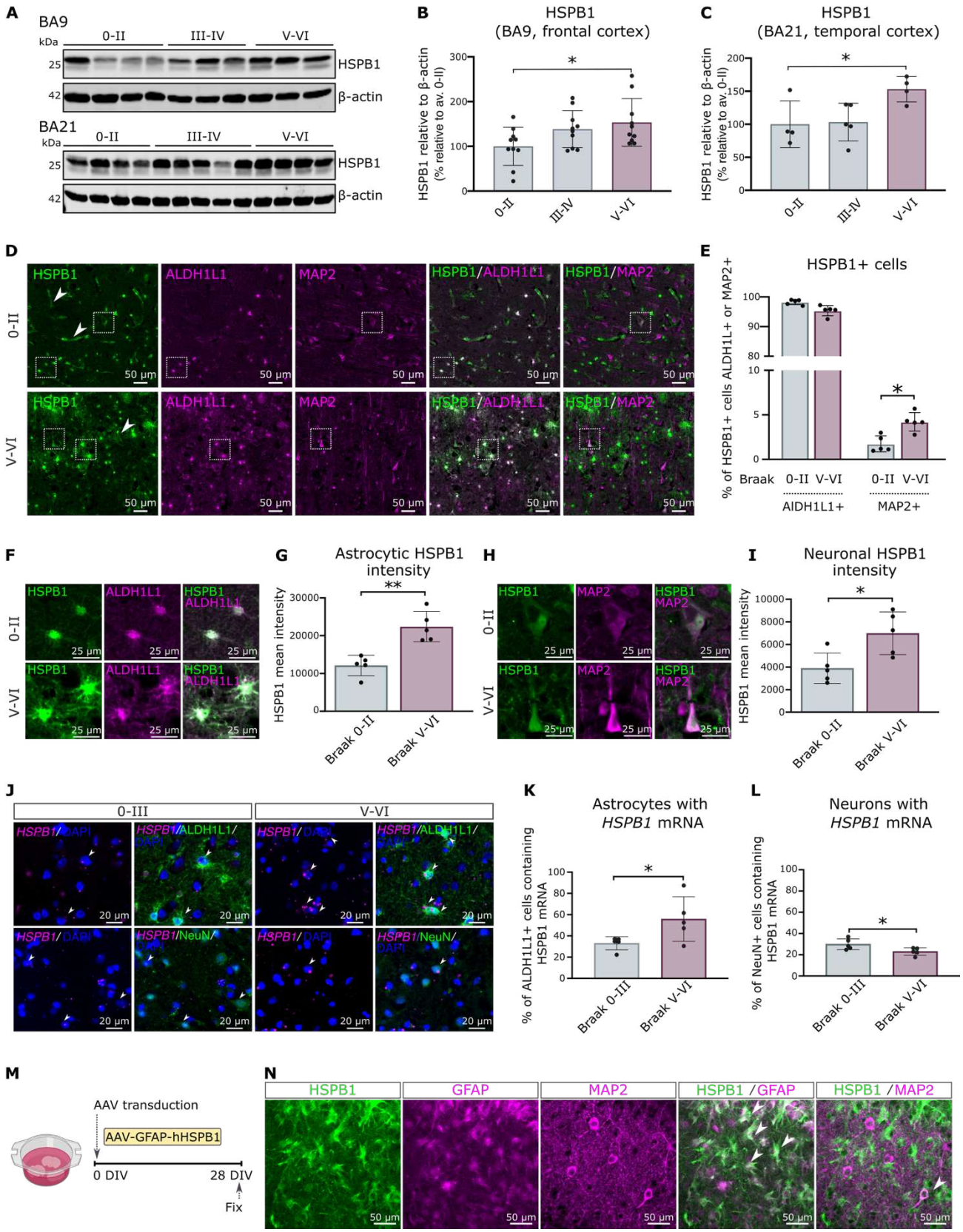

A
BA9
kDa
0-II
III-IV
V-VI
25
42
HSPB1
β-actin
BA21
B
HSPB1
(BA9, frontal cortex)
HSPB1 relative to β-actin
(% relative to av. 0-II)
C
HSPB1
(BA21, temporal cortex)
D
HSPB1
ALDH1L1
MAP2
HSPB1/ALDH1L1
HSPB1/MAP2
50 µm
E
HSPB1+ cells
% of HSPB1+ cells ALDH1L+ or MAP2+
Braak
AlDH1L1+
MAP2+
F
25 µm
G
Astrocytic HSPB1
intensity
HSPB1 mean intensity
Braak 0-II
Braak V-VI
H
I
Neuronal HSPB1
intensity
J
0-III
V-VI
HSPB1/DAPI
HSPB1/ALDH1L1/
DAPI
HSPB1/NeuN/
DAPI
20 µm
K
Astrocytes with
HSPB1 mRNA
% of ALDH1L1+ cells containing
HSPB1 mRNA
Braak 0-III
L
Neurons with
HSPB1 mRNA
% of NeuN+ cells containing
M
AAV transduction
AAV-GFAP-hHSPB1
0 DIV
28 DIV
Fix
N
GFAP
HSPB1 /GFAP
HSPB1 /MAP2

Figure 2

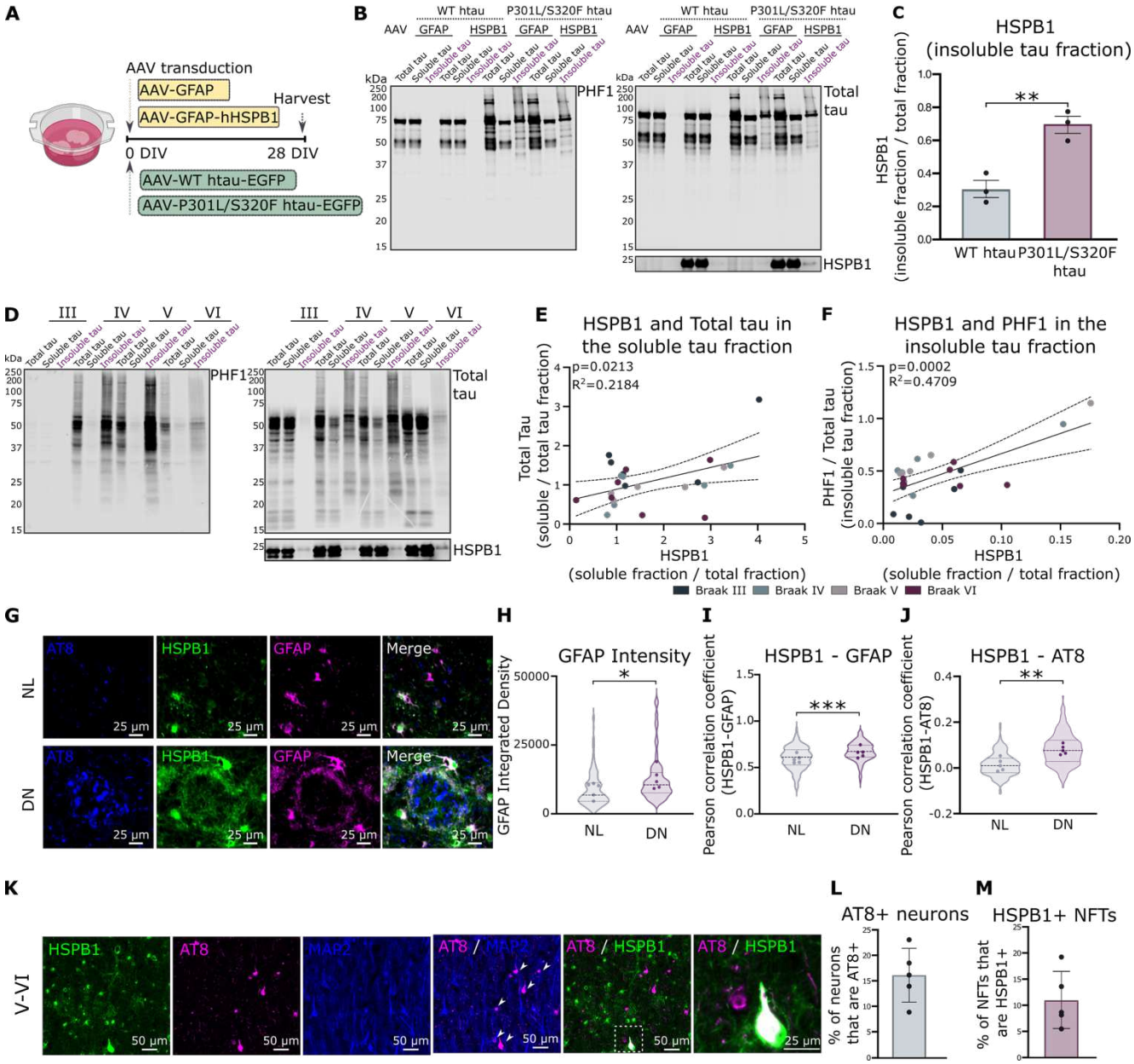

A
AAV transduction
AAV-GFAP
AAV-GFAP-hHSPB1
Harvest
0 DIV
28 DIV
AAV-WT htau-EGFP
AAV-P301L/S320F htau-EGFP
B
WT htau
P301L/S320F htau
AAV GFAP HSPB1 GFAP HSPB1
Total tau
Soluble tau
Insoluble tau
kDa
PHF1
Total tau
HSPB1
C
HSPB1
(insoluble tau fraction)
HSPB1
(insoluble fraction / total fraction)
**
WT htau
P301L/S320F htau
D
III IV V VI
PHF1
Total tau
HSPB1
E
HSPB1 and Total tau in the soluble tau fraction
p=0.0213
R²=0.2184
Total Tau
(soluble / total tau fraction)
HSPB1
(soluble fraction / total fraction)
F
HSPB1 and PHF1 in the insoluble tau fraction
p=0.0002
R²=0.4709
PHF1 / Total tau
(insoluble tau fraction)
HSPB1
(soluble fraction / total fraction)
Braak III
Braak IV
Braak V
Braak VI
G
NL
DN
AT8
HSPB1
GFAP
Merge
25 µm
H
GFAP Intensity
GFAP Integrated Density
*
NL
DN
I
HSPB1 - GFAP
Pearson correlation coefficient
(HSPB1-GFAP)
***
NL
DN
J
HSPB1 - AT8
Pearson correlation coefficient
(HSPB1-AT8)
**
NL
DN
K
V-VI
HSPB1
AT8
MAP2
AT8 / MAP2
AT8 / HSPB1
50 µm
25 µm
L
AT8+ neurons
% of neurons that are AT8+
M
HSPB1+ NFTs
% of NFTs that are HSPB1+

Figure 3

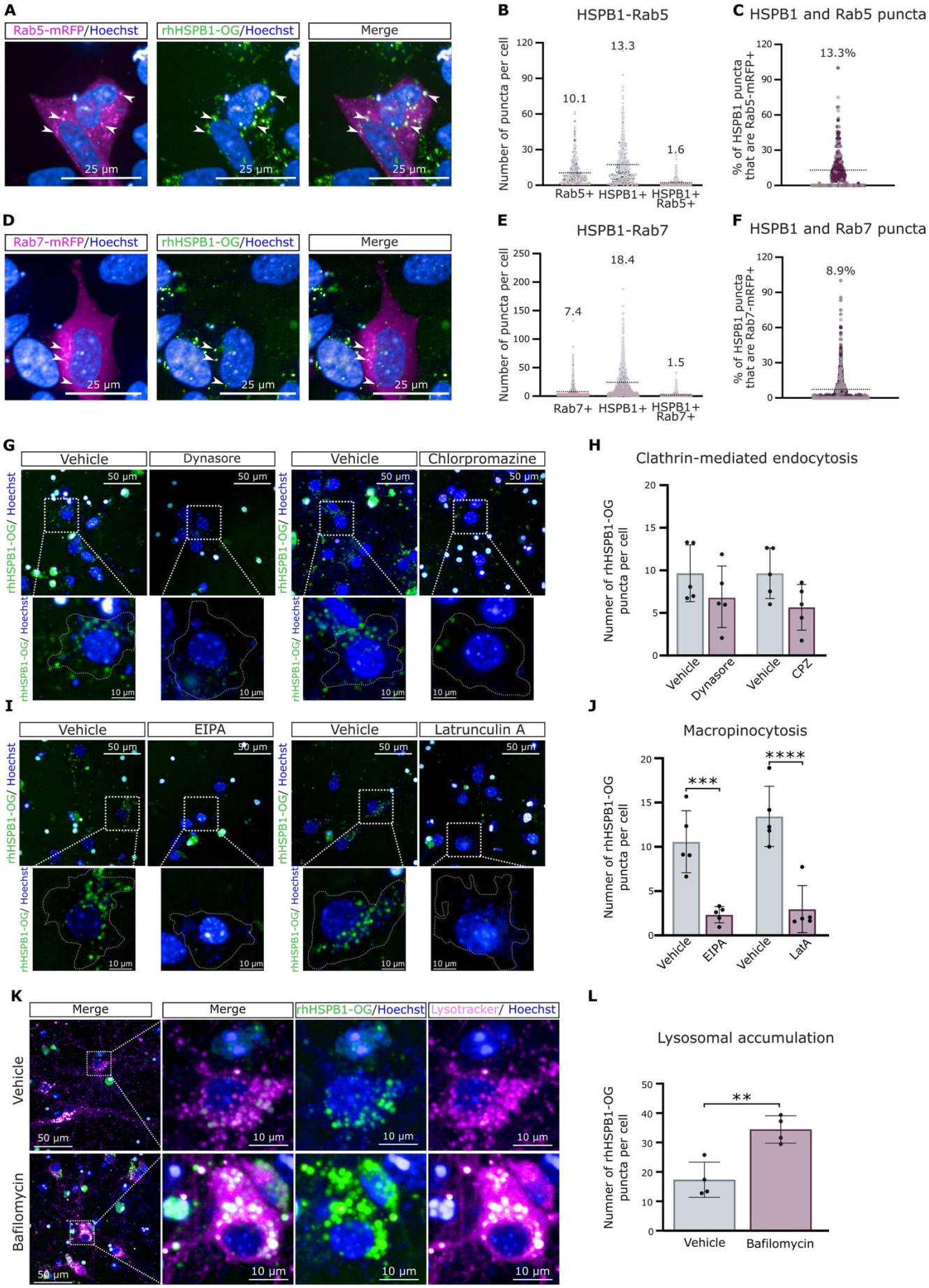

A
Rab5-mRFP/Hoechst
rhHSPB1-OG/Hoechst
Merge
25 µm
B
HSPB1-Rab5
Number of puncta per cell
10.1
13.3
1.6
Rab5+
HSPB1+
HSPB1+ Rab5+
C
HSPB1 and Rab5 puncta
% of HSPB1 puncta that are Rab5-mRFP+
13.3%
D
Rab7-mRFP/Hoechst
rhHSPB1-OG/Hoechst
Merge
E
HSPB1-Rab7
7.4
18.4
1.5
Rab7+
HSPB1+
HSPB1+ Rab7+
F
HSPB1 and Rab7 puncta
8.9%
G
Vehicle
Dynasore
Chlorpromazine
rhHSPB1-OG/ Hoechst
50 µm
10 µm
H
Clathrin-mediated endocytosis
Numner of rhHSPB1-OG puncta per cell
Vehicle
Dynasore
CPZ
I
EIPA
Latrunculin A
J
Macropinocytosis
***
****
LatA
K
Merge
rhHSPB1-OG/Hoechst
Lysotracker/ Hoechst
Vehicle
Bafilomycin
L
Lysosomal accumulation
**

Figure 4

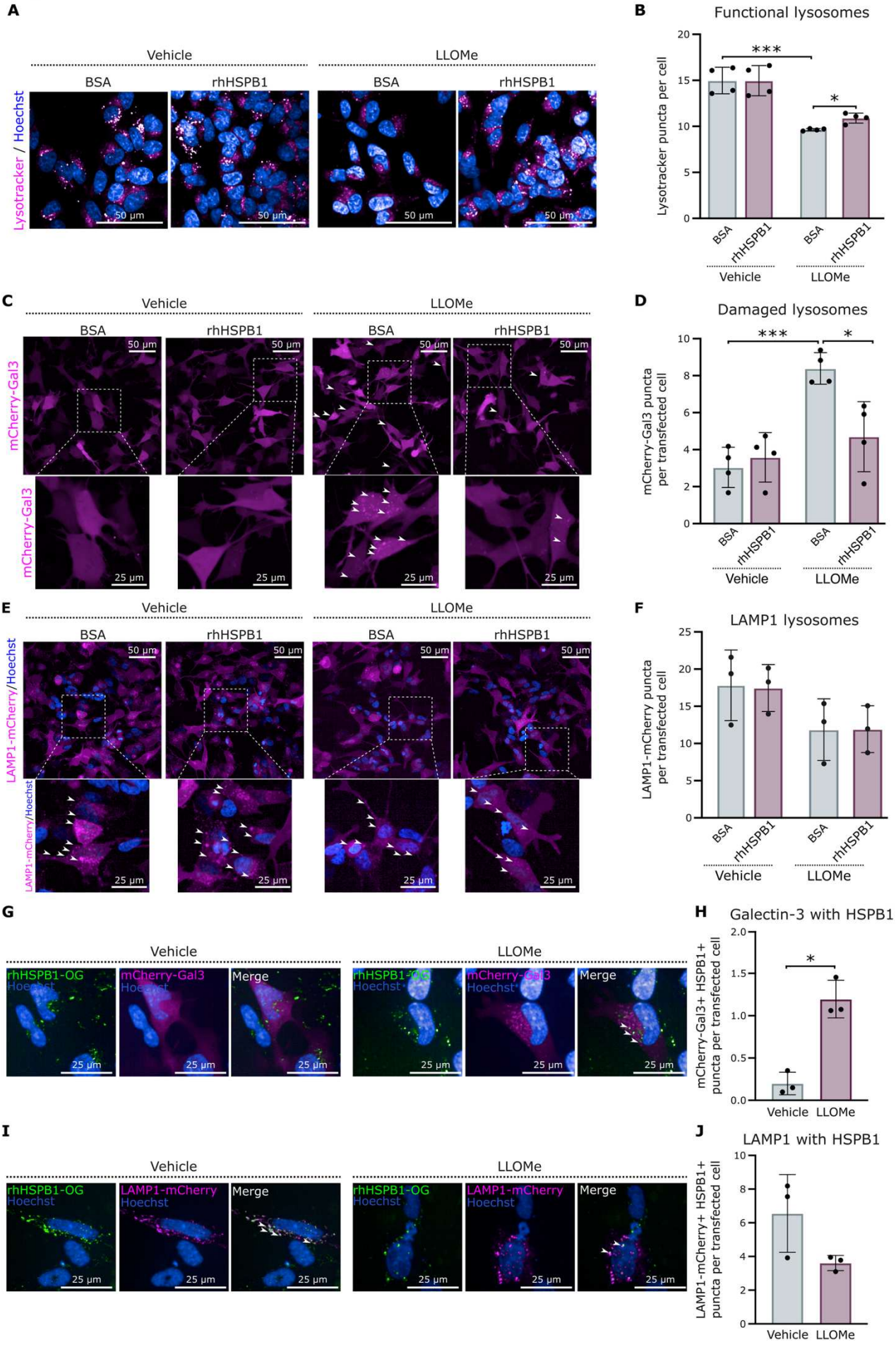

A
Vehicle
LLOMe
BSA
rhHSPB1
BSA
rhHSPB1
Lysotracker / Hoechst
50 µm
B
Functional lysosomes
Lysotracker puncta per cell
***
*
BSA
rhHSPB1
BSA
rhHSPB1
Vehicle
LLOMe
C
Vehicle
LLOMe
BSA
rhHSPB1
BSA
rhHSPB1
mCherry-Gal3
mCherry-Gal3
25 µm
D
Damaged lysosomes
mCherry-Gal3 puncta per transfected cell
***
*
Vehicle
LLOMe
E
Vehicle
LLOMe
LAMP1-mCherry/Hoechst
LAMP1-mCherry/Hoechst
25 µm
F
LAMP1 lysosomes
LAMP1-mCherry puncta per transfected cell
Vehicle
LLOMe
G
Vehicle
LLOMe
rhHSPB1-OG
Hoechst
mCherry-Gal3
Merge
25 µm
H
Galectin-3 with HSPB1
mCherry-Gal3+ HSPB1+ puncta per transfected cell
*
Vehicle
LLOMe
I
Vehicle
LLOMe
rhHSPB1-OG
Hoechst
LAMP1-mCherry
Merge
25 µm
J
LAMP1 with HSPB1
LAMP1-mCherry+ HSPB1+ puncta per transfected cell
Vehicle
LLOMe

Figure 5

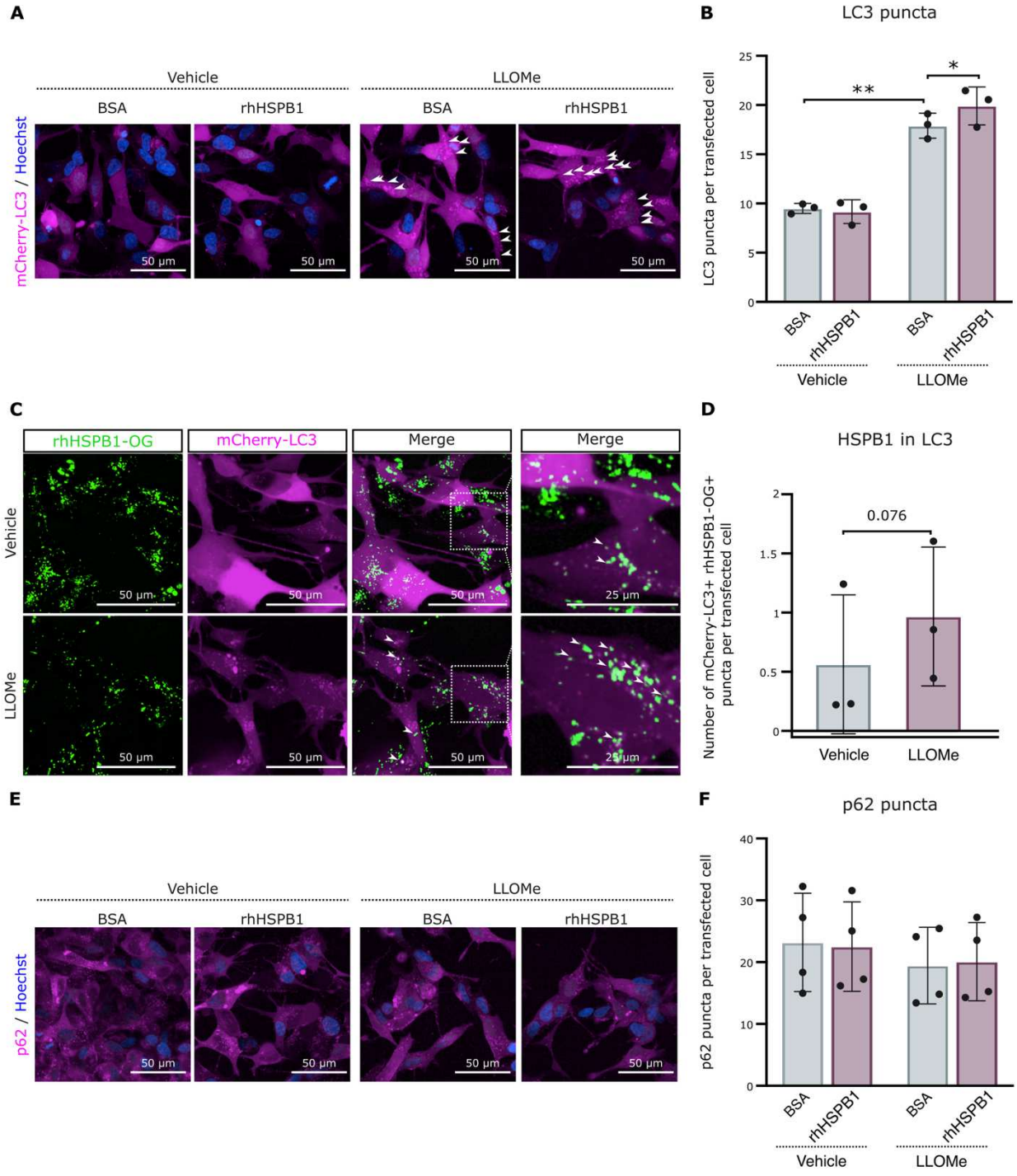

A
Vehicle
LLOMe
BSA
rhHSPB1
BSA
rhHSPB1
mCherry-LC3 / Hoechst
50 µm
B
LC3 puncta
LC3 puncta per transfected cell
**
*
BSA
rhHSPB1
BSA
rhHSPB1
Vehicle
LLOMe
C
rhHSPB1-OG
mCherry-LC3
Merge
Merge
Vehicle
LLOMe
50 µm
25 µm
D
HSPB1 in LC3
Number of mCherry-LC3+ rhHSPB1-OG+ puncta per transfected cell
0.076
Vehicle
LLOMe
E
Vehicle
LLOMe
BSA
rhHSPB1
BSA
rhHSPB1
p62 / Hoechst
50 µm
F
p62 puncta
p62 puncta per transfected cell
BSA
rhHSPB1
BSA
rhHSPB1
Vehicle
LLOMe

Figure 6

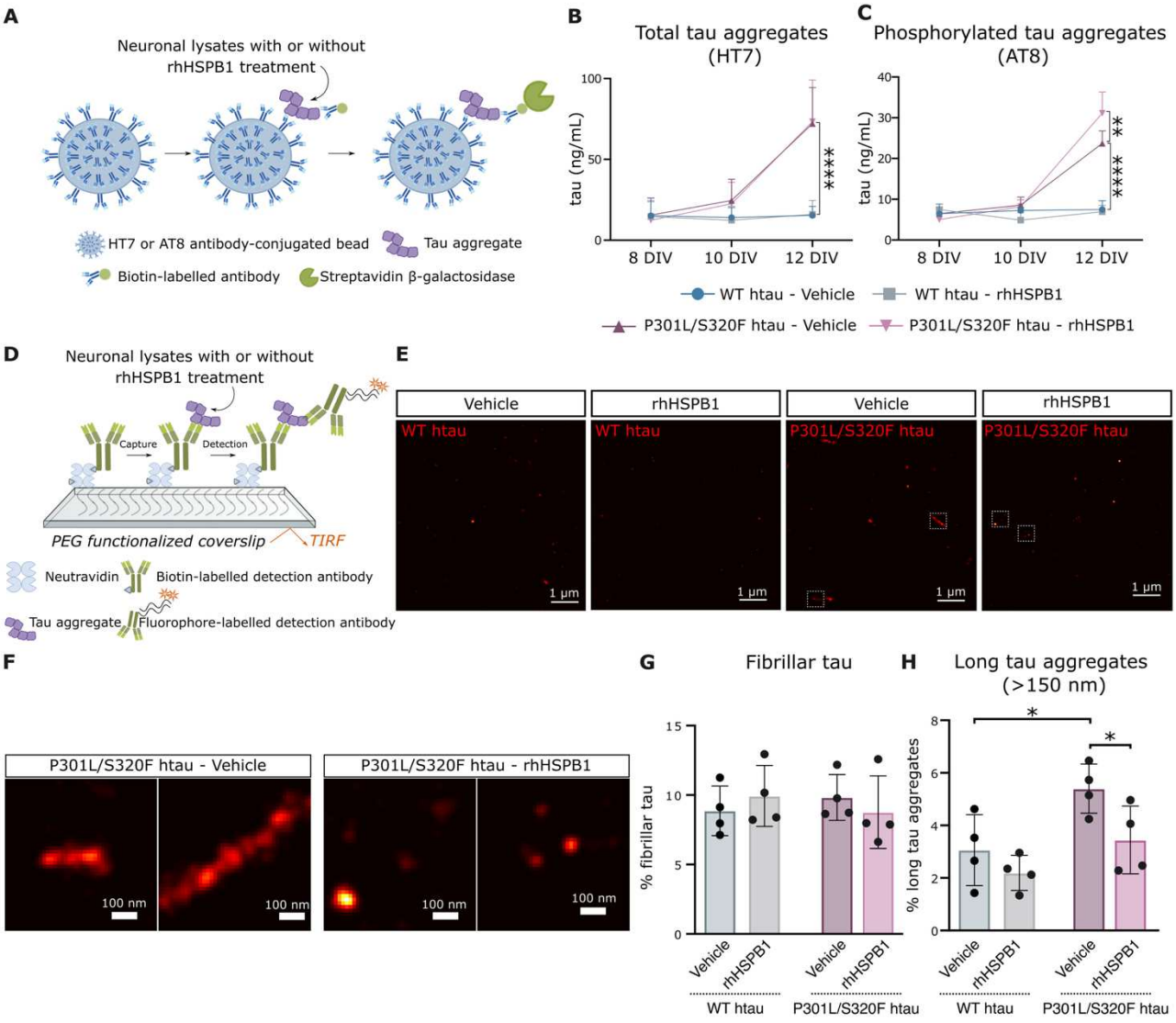

A
Neuronal lysates with or without rhHSPB1 treatment
HT7 or AT8 antibody-conjugated bead
Tau aggregate
Biotin-labelled antibody
Streptavidin β-galactosidase
B
Total tau aggregates (HT7)
tau (ng/mL)
8 DIV
10 DIV
12 DIV
****
C
Phosphorylated tau aggregates (AT8)
**
****
WT htau - Vehicle
WT htau - rhHSPB1
P301L/S320F htau - Vehicle
P301L/S320F htau - rhHSPB1
D
Neuronal lysates with or without rhHSPB1 treatment
Capture
Detection
PEG functionalized coverslip
TIRF
Neutravidin
Biotin-labelled detection antibody
Tau aggregate
Fluorophore-labelled detection antibody
E
Vehicle
rhHSPB1
Vehicle
rhHSPB1
WT htau
WT htau
P301L/S320F htau
P301L/S320F htau
1 µm
F
P301L/S320F htau - Vehicle
P301L/S320F htau - rhHSPB1
100 nm
G
Fibrillar tau
% fibrillar tau
Vehicle
rhHSPB1
WT htau
P301L/S320F htau
H
Long tau aggregates (>150 nm)
% long tau aggregates
*
*

Figure 7

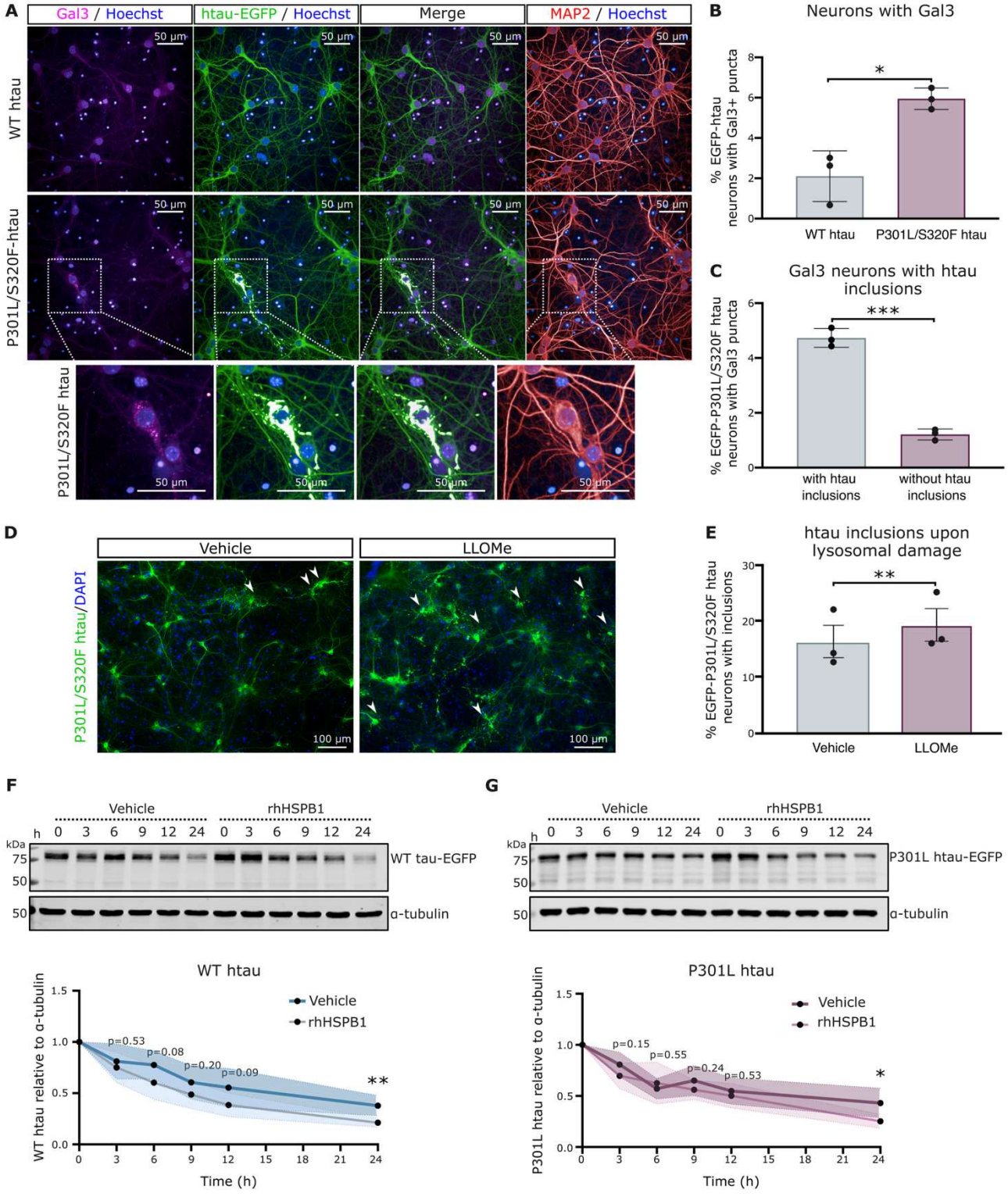
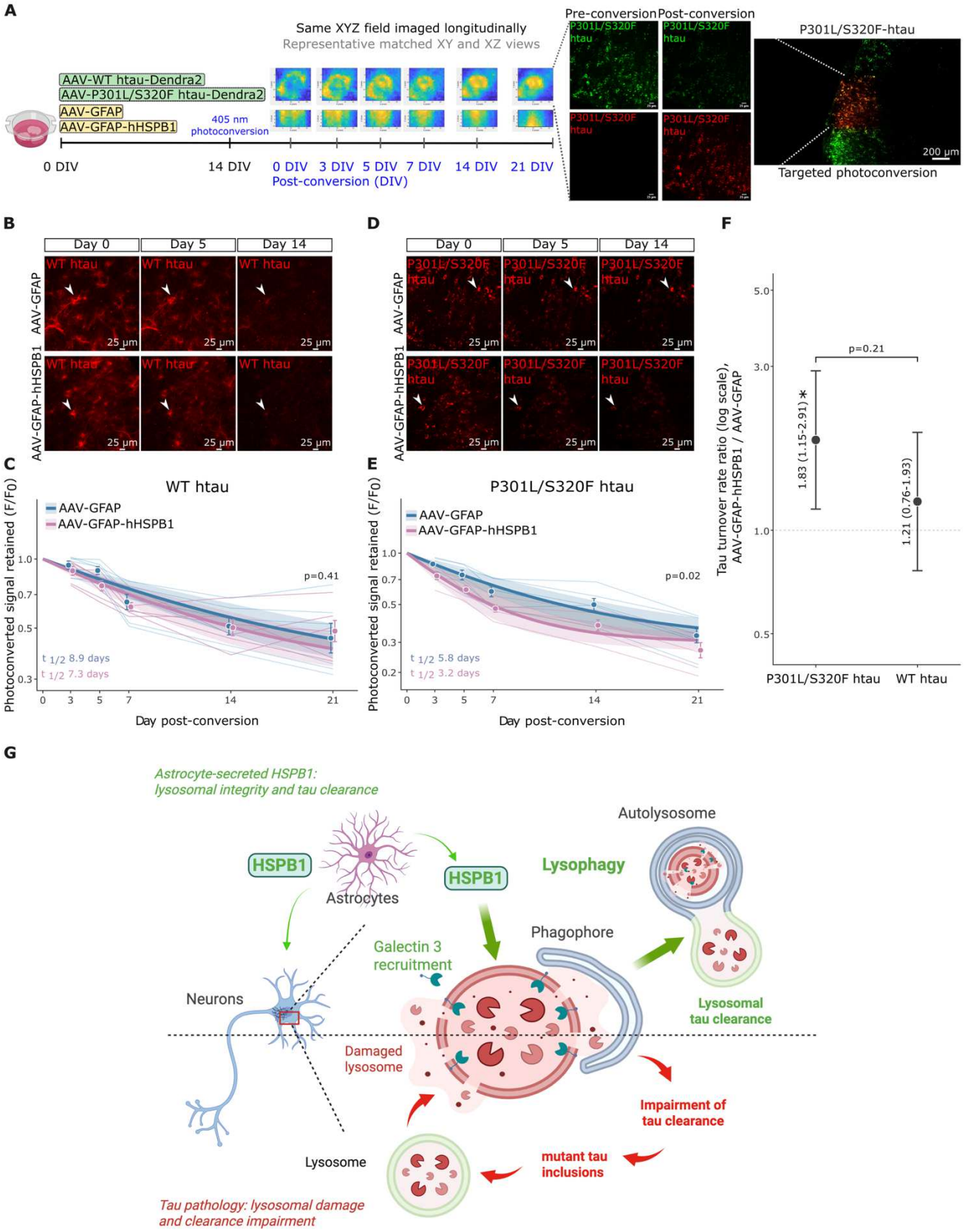

A
Gal3 / Hoechst
htau-EGFP / Hoechst
Merge
MAP2 / Hoechst
WT htau
P301L/S320F-htau
P301L/S320F htau
50 µm
B
Neurons with Gal3
% EGFP-htau neurons with Gal3+ puncta
WT htau
P301L/S320F htau
C
Gal3 neurons with htau inclusions
% EGFP-P301L/S320F htau neurons with Gal3 puncta
with htau inclusions
without htau inclusions
D
Vehicle
LLOMe
P301L/S320F htau/DAPI
100 µm
E
htau inclusions upon lysosomal damage
% EGFP-P301L/S320F htau neurons with inclusions
Vehicle
LLOMe
F
Vehicle
rhHSPB1
h 0 3 6 9 12 24 0 3 6 9 12 24
kDa
75
50
WT tau-EGFP
α-tubulin
WT htau
WT htau relative to α-tubulin
Vehicle
rhHSPB1
p=0.53
p=0.08
p=0.20
p=0.09
Time (h)
G
Vehicle
rhHSPB1
h 0 3 6 9 12 24 0 3 6 9 12 24
kDa
75
50
P301L htau-EGFP
α-tubulin
P301L htau
P301L htau relative to α-tubulin
Vehicle
rhHSPB1
p=0.15
p=0.55
p=0.24
p=0.53
Time (h)

Figure 8


A
Same XYZ field imaged longitudinally
Representative matched XY and XZ views
AAV-WT htau-Dendra2
AAV-P301L/S320F htau-Dendra2
AAV-GFAP
AAV-GFAP-hHSPB1
405 nm photoconversion
0 DIV
14 DIV
0 DIV 3 DIV 5 DIV 7 DIV 14 DIV 21 DIV
Post-conversion (DIV)
Pre-conversion
Post-conversion
P301L/S320F htau
P301L/S320F-htau
200 µm
Targeted photoconversion
B
Day 0
Day 5
Day 14
AAV-GFAP
AAV-GFAP-hHSPB1
WT htau
25 µm
D
P301L/S320F htau
C
WT htau
Photoconverted signal retained (F/F0)
AAV-GFAP
AAV-GFAP-hHSPB1
p=0.41
t 1/2 8.9 days
t 1/2 7.3 days
Day post-conversion
E
P301L/S320F htau
p=0.02
t 1/2 5.8 days
t 1/2 3.2 days
F
Tau turnover rate ratio (log scale), AAV-GFAP-hHSPB1 / AAV-GFAP
p=0.21
1.83 (1.15-2.91) *
1.21 (0.76-1.93)
P301L/S320F htau
WT htau
G
Astrocyte-secreted HSPB1: lysosomal integrity and tau clearance
HSPB1
Astrocytes
Autolysosome
Lysophagy
Phagophore
Galectin 3 recruitment
Neurons
Lysosomal tau clearance
Damaged lysosome
Impairment of tau clearance
Lysosome
mutant tau inclusions
Tau pathology: lysosomal damage and clearance impairment

Supplementary Files

This is a list of supplementary files associated with this preprint. Click to download.

- BeltranLoboetal.SupplementaryInformation260927.pdf
- WBuncroppedmembranes.pdf